The central engine of GRB 130831A and the energy breakdown of a relativistic explosion

M. De Pasquale,[1,2,3]★ S. R. Oates,[1,4] J. L. Racusin,[5] D. A. Kann,[6] B. Zhang,[7]
A. Pozanenko,[8,9] A. A. Volnova,[8] A. Trotter,[10] N. Frank,[10] A. Cucchiara,[5] E. Troja,[5]
B. Sbarufatti,[11] N. R. Butler,[12] S. Schulze,[13,14] Z. Cano,[15]★ M. J. Page,[1]
A. J. Castro-Tirado,[4,16] J. Gorosabel,[4,17,18]† A. Lien,[5,19] O. Fox,[20] O. Littlejohns,[12]
J. S. Bloom,[20] J. X. Prochaska,[21] J. A. de Diego,[22] J. Gonzalez,[22] M. G. Richer,[23]
C. Román-Zúñiga,[23] A. M. Watson,[22] N. Gehrels,[5] H. Moseley,[5] A. Kutyrev,[5]
S. Zane,[1] V. Hoette,[24] R. R. Russell,[24] V. Rumyantsev,[25] E. Klunko,[26]
O. Burkhonov,[27] A. A. Breeveld,[1] D. E. Reichart[10] and J. B. Haislip[10]

Affiliations are listed at the end of the paper

ABSTRACT

Gamma-ray bursts (GRBs) are the most luminous explosions in the Universe, yet the nature and physical properties of their energy sources are far from understood. Very important clues, however, can be inferred by studying the afterglows of these events. We present optical and X-ray observations of GRB 130831A obtained by *Swift*, *Chandra*, Skynet, Reionization And Transients Infra-Red camera, Maidanak, International Scientific Optical-Observation Network, Nordic Optical Telescope, Liverpool Telescope and Gran Telescopio Canarias. This burst shows a steep drop in the X-ray light curve at $\simeq 10^5$ s after the trigger, with a power-law decay index of $\alpha \sim 6$. Such a rare behaviour cannot be explained by the standard forward shock (FS) model and indicates that the emission, up to the fast decay at 10^5 s, must be of 'internal origin', produced by a dissipation process within an ultrarelativistic outflow. We propose that the source of such an outflow, which must produce the X-ray flux for $\simeq 1$ d in the cosmological rest frame, is a newly born magnetar or black hole. After the drop, the faint X-ray afterglow continues with a much shallower decay. The optical emission, on the other hand, shows no break across the X-ray steep decrease, and the late-time decays of both the X-ray and optical are consistent. Using both the X-ray and optical data, we show that the emission after $\simeq 10^5$ s can be explained well by the FS model. We model our data to derive the kinetic energy of the ejecta and thus measure the efficiency of the central engine of a GRB with emission of internal origin visible for a long time. Furthermore, we break down the energy budget of this GRB into the prompt emission, the late internal dissipation, the kinetic energy of the relativistic ejecta, and compare it with the energy of the associated supernova, SN 2013 fu.

Key words: radiation mechanisms: non-thermal – shock waves – gamma-ray burst: general – gamma-ray burst: individual: GRB 130831A – stars: magnetars.

1 INTRODUCTION

The study of gamma-ray bursts (GRBs) has received an exceptional boost thanks to the *Swift* mission (Gehrels et al. 2004), which has enabled rapid follow-up radio to X-ray observations of GRBs.

However, despite a very large number of such fast follow-up observations performed by this spacecraft and by ground observatories, the characteristics of the 'central engine' that produces the GRB are still unclear. The prevailing model (Woosley 1993; MacFadyen & Woosley 1999; MacFadyen, Woosley & Heger 2001; Thompson 2007) predicts the formation of a compact object, either a black hole or a magnetar, surrounded by an accretion disc. The compact object is the result of the core collapse of a very massive star or the final merger of two neutron stars (NS–NS) or NS – black hole

binary. Under the correct conditions of angular momentum and magnetic field, such a system would launch a collimated, ultrarelativistic jet (e.g. via the Blanford–Znajek mechanism; Blandford & Znajek 1977). Within these jets, one or more 'internal dissipation' processes take place (for some reviews, see Kumar & Zhang 2015 and Zhang 2011), converting part of the kinetic and/or magnetic energy into radiation. A burst of gamma-rays will then be visible if the observer is placed within the opening angle of the outflow.

Following the prompt gamma-ray emission, long-lived afterglow emission is detected in several energy bands (radio, optical, X-ray and probably high-energy gamma-rays). The consensus is that the afterglow radiation is emitted when ultrarelativistic ejecta interact with the circumburst medium, driving a forward shock (FS), which moves into the medium, and a reverse shock (RS), which propagates backwards through the ejecta. In particular, the emission due to the FS can in principle last indefinitely. A hallmark of RS and FS afterglow emission is that the flux density F_ν behaves as a power law both in time and frequency, being described as $F_\nu \propto t^{-\alpha} \nu^{-\beta}$, where t is the time from the GRB trigger (Kobayashi & Zhang 2007) and ν is the frequency.

However, *Swift* observations have produced evidence of more complex phenomena during the afterglow phase, such as X-ray and optical flares (Falcone et al. 2007; Margutti et al. 2011; Swenson et al. 2013), that cannot be attributed to the FS due to their fast temporal variability. For a few kiloseconds (ks) after the trigger, the afterglow flux often decays in a slow fashion (phase II of the canonical X-ray Telescope (XRT) light curve, also known as 'plateau'; Nousek et al. 2006; O'Brien et al. 2006; Racusin et al. 2009; Margutti et al. 2011) which cannot be understood if the fireball follows an adiabatic evolution; a process of energy injection (Zhang et al. 2006) into the fireball is usually invoked to explain such a feature. These observations strongly suggest that the GRB central engine is still active, and produces energy and/or a relativistic outflow.

In a small subset of *Swift* GRB afterglows, observations have shown slow decline phases of the X-ray flux which terminate with an abrupt fall in the emission, with slopes $\alpha \gtrsim 3$–4, sometimes approaching $\alpha \simeq 9$–10 (Liang, Zhang & Zhang 2007; Troja et al. 2007; Lyons et al. 2010; Rowlinson et al. 2013; Lü & Zhang 2014). Again, the FS model does not predict such behaviour. Instead, such steep decay can be expected when the central engine is a newly born magnetar, which emits a very high luminosity outflow due to the spin-down process (Usov 1992; Zhang & Mészáros 2001, 2002; Dall'Osso et al. 2011), which in turn produces emission we can directly observe in the X-ray. A very energetic outflow could also be produced by a newly formed stellar mass black hole surrounded by an accretion disc. The electromagnetic luminosity is expected to fall rapidly after the time-scale T_{em} of the spin-down process, if the magnetar collapses into a black hole, or accretion on to the black hole stops.

The outflow produced by the spin-down process should generate emission via the synchrotron process. This kind of emission seems to be produced mostly in the X-ray band, while it is not usually detected at lower frequencies such as the optical (see Troja et al. 2007; Zhang et al. 2009; Rowlinson et al. 2013; however, see Cano et al. 2014 for GRB130215A), perhaps because the optical band is at or below the synchrotron self-absorption frequency (Zhang 2009; see also Shen & Zhang 2009). At low frequencies, the dominant emission mechanism seems to be the standard FS, with its power-law decays and slow flux variations. FS emission, however, is still expected to be present even in the X-ray band, and it should emerge once the X-ray emission from the outflow produced by the magnetar
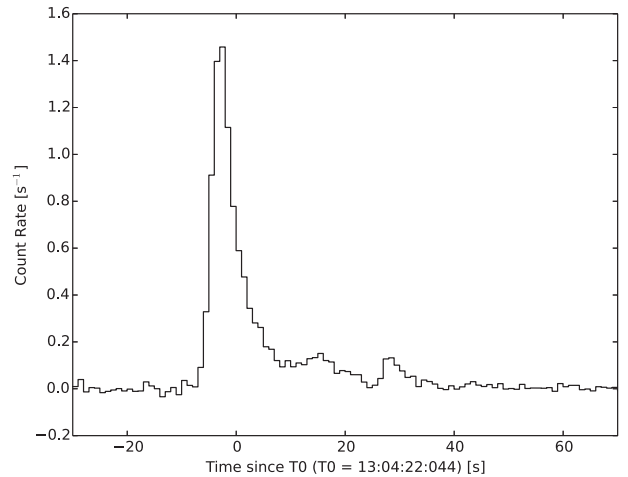

Figure 1. *Swift* BAT light curve of the prompt emission from GRB 130831A.

or the black hole drops. So far, this has been seen clearly in the case of the long GRB 070110 (Troja et al. 2007). In this event, the X-ray light-curve showed a plateau lasting for 20 ks, after which the flux fell quickly with a slope of $\alpha \sim 9$, and then resumed a power-law decay with a much shallower slope of $\alpha \sim 1$. Such a late slope appears in most GRB afterglows and is likely produced by the FS.

In this paper, we present the well-sampled X-ray, UV/Optical and NIR observations of the afterglow of GRB 130831A, and show that its behaviour can be interpreted as a superposition of FS emission and 'internal emission', the latter of which suddenly ceases at $\simeq 100$ ks. This article is organized as follows. In Section 2, we present the observations taken by different instruments and observing facilities, and show how the data were reduced and analysed. We recall the results of the observations taken by other groups on GRB130831A as well. In Section 3, we show and fit the resulting light curves and spectral energy distributions (SEDs) of this GRB. In Section 4, we model the afterglow of GRB 130831A in the context of FS and internal emission models, we discuss the possible origins of the observed emission and the properties of the object that produced the explosion. Finally, we present our conclusions in Section 5. Throughout the paper, errors are expressed at the 1σ confidence level (CL) unless stated otherwise, and we assume a Λ cold dark matter Cosmology with $H_0 = 70$ km s^{-1} Mpc^{-1}, $\Omega_m = 0.27$ and $\Omega_\Lambda = 0.73$ (Jarosik et al. 2011).

2 OBSERVATIONS AND ANALYSIS

2.1 X-ray data

2.1.1 Swift-*BAT*

The *Swift* Burst Alert Telescope (BAT; Barthelmy et al. 2005) triggered on GRB 130831A at $T_0 =$ 13:04:16.54 UT, 2013 August 31. The mask-weighted light-curve in the 15–350 keV energy range (see Fig. 1) shows a main pulse with a fast rise and exponential decay (FRED) shape. It starts at T_0-2 s and peaks at T_0+3 s. The major pulse structure ends at T_0+12 s. However, there is some extended emission that lasts until T_0+41 s, with two additional peaks at T_0+20 s and T_0+32 s. T_{90} (15–350 keV), the interval during which from 5 to 95 per cent of the total emission is recorded, is 30.2 ± 1.4 s (error includes systematics).
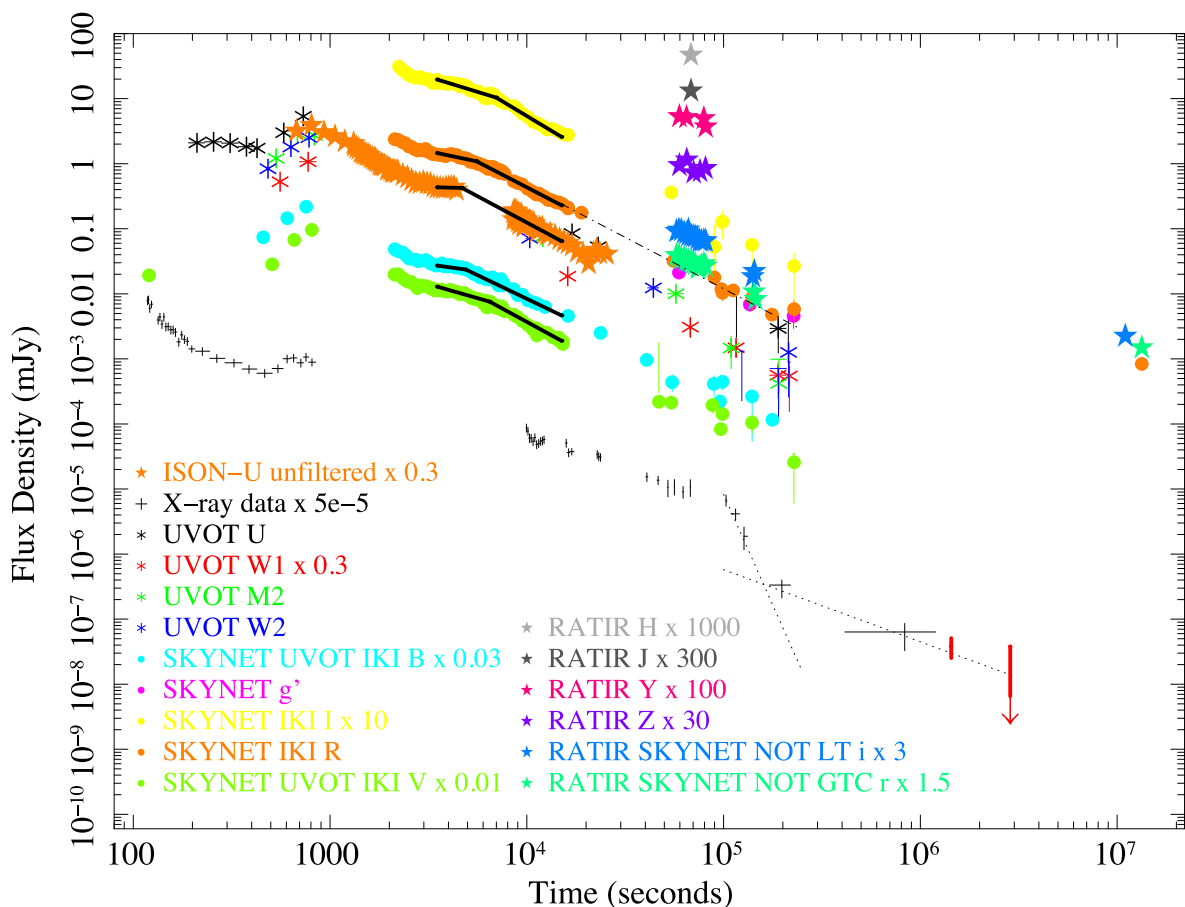
Figure 2. GRB 130831A light curves in near-infrared, optical, UV and X-ray band. Black crosses are XRT data points, while red ones are *Chandra* data points. Data between 230 and 6000 ks are contaminated or dominated by the emission of the SN associated with this GRB and are not shown here. Data points at $\simeq 10^7$ s show the brightness of the host galaxy. The reader is referred to Cano et al. (2014) for a complete study of the SN. We plot the broken power-law models on the unfiltered and *BVRI* light curves between 3.5 and 15 ks (solid lines), the power-law model on the *R* light curve between 15 and 230 ks (dot–dashed line), the two power-law model on the X-ray that fits the data in this band after 100 ks (dotted lines). See Tables 2 and 6 for the values of the parameters. UV/optical/NIR data have not been corrected for Galactic and host galaxy extinction.

The time-averaged spectrum between $T_0 - 1.9$ s and $T_0 + 41.4$ s can be fitted by a simple power-law model with a spectral index $\beta = 0.93 \pm 0.03$ ($\chi^2 = 56.7$ for 57 degrees of freedom, dof) in the energy band 15–150 keV. This model gives a fluence of $(6.49 \pm 0.09) \times 10^{-6}$ erg cm^{-2} in the same energy range. The 1-s peak spectrum can also be fitted by a simple power-law model with $\beta = 0.70 \pm 0.05$ ($\chi^2/\mathrm{dof} = 56.4/57$) in the energy band 15–150 keV, which gives a peak flux of $9.44 \pm 0.25 \times 10^{-7}$ erg cm^{-2} s^{-1} in the same band. The BAT analysis uses the event data from $T_0 - 240$ s to $T_0 + 963$ s.

2.1.2 Swift-*XRT observations*

After the BAT trigger, the *Swift* satellite promptly slewed to point the narrow field instruments at the source. The XRT (Burrows et al. 2005) began observations of GRB 130831A 125.8 s after the trigger in the 0.3–10 keV energy band. The XRT monitored the source until 2013 September 14, collecting 84.9 s of data in Window Timing (WT) mode (11.6 s were taken while the spacecraft was settling and the remaining 73.3 s pointing mode) and 59.7 ks in Photon Counting (PC) mode.

XRT data were processed using the HEASOFT software packages,[1] version 6.15 and version 20130313 of the XRT Calibration DataBase,[2] applying calibrations and standard filtering and screening criteria (for more details see Evans et al. 2009). WT data were extracted in an interval centred on the source, 20 pixels on each side, and the background estimated using intervals between 40 and 60 pixels from the source. The PC data were initially affected by pile-up, and corrected by excluding the central core of 6 pixel radius. The remaining PC data were extracted using a circular region with 30-pixel radius, and when the count rate dropped below 10^{-2} counts s^{-1}, within a 10 pixel radius. During the extraction of the light curve, a minimum signal-to-noise ratio (S/N) criterion was applied for the re-binning, such that we required an S/N greater than 3 for all data points, with the exception of the last data point. The 90 per cent CL intervals were estimated following the Kraft, Burrows & Nousek (1991) technique for low count rate sources. The X-ray light curve (Fig. 2), which shows the temporal evolution of the flux, was constructed once the spectral information was obtained (see Sections 3.1 and 3.2, Tables 1 and 2).

[1] http://heasarc.nasa.gov/lheasoft/
[2] www.swift.ac.uk/analysis/xrt/files/SWIFT-XRT-CALDB-09_v17.pdf

Table 1. Time resolved spectral analysis. ST = settling exposure, WT = Window Timing exposure, PC = Photon Counting exposure. Note: errors are at 90 per cent C.L.

Name	Start time (s)	End time (s)	Excess N_H (10^{20} cm^{-2})	β	Observed flux ($\times$ erg cm^{-2} s^{-1})	Unabsorbed flux ($\times$ erg cm^{-2} s^{-1})	Cstat	dof
ST	115.8	125.2	<700	1.7 ± 0.2	7.93×10^{-10}	1.06×10^{-9}	125.4	146
WT1	132.0	157.9	<400	1.7 ± 0.1	6.91×10^{-10}	9.21×10^{-10}	163.3	159
WT2	157.9	205.6	<500	1.3 ± 0.1	3.34×10^{-10}	4.06×10^{-10}	182.2	184
PC1	207.2	287.2	<500	1.2 ± 0.3	1.70×10^{-10}	2.03×10^{-10}	82.5	76
PC2	287.2	367.2	<100	0.7 ± 0.3	1.47×10^{-10}	1.61×10^{-10}	60.3	60
PC3	367.2	437.2	<20	1.1 ± 0.4	9.69×10^{-11}	1.14×10^{-10}	37.1	41
PC4	437.2	847.2	<900	0.8 ± 0.1	1.47×10^{-10}	1.63×10^{-10}	199.4	216
PC5	9891.6	132 418.7	$6.8^{+5.4}_{-5.1}$	0.77 ± 0.12	6.23×10^{-11}	6.55×10^{-11}	305.4	367
PC6	171 385.0	1193 789.0	<700	1.0 ± 0.9	1.52×10^{-14}	1.80×10^{-14}	10.3	17

Table 2. Results of the temporal analysis of the X-ray emission of GRB 130831A, which includes XRT and *Chandra* data. We show the results of fitting the data with two models. The first model, BPLs + flare, consists of power-law plus broken power-law plus power-law plus Gaussian flare and it fits the whole X-ray data set. The second model, *2powls*, includes 2 power-law components and it fits the data after 100 ks. We show the decay indices, break time and the centre (GC), width (GW) and flux normalization (GN) of the Gaussian flare, of the first model. The latter model has $\alpha_{X,3}$ and $\alpha_{X,4}$ only.

Model	$\alpha_{X,1}$ (ks)	$\alpha_{X,2}$ (ks)	t_b	$\alpha_{X,3}$ (ks)	GC (ks)	GW ($\times 10^{-11}$ erg cm^{-2} s^{-1})	GN	$\alpha_{X,4}$	χ^2/dof
BPLs + flare	5.97 ± 0.01	$0.80^{+0.01}_{-0.02}$	$98.26^{+2.94}_{-3.30}$	$5.9^{+1.0}_{-0.4}$	0.73 ± 0.03	0.11 ± 0.02	11.2 ± 1.6	$0.90^{+0.11}_{-0.05}$	50.7/48
2powls			$6.8^{+2.0}_{-1.5}$					$1.11^{+0.22}_{-0.29}$	2.4/3

2.1.3 Chandra observations

After the very steep break, we requested and obtained two *Chandra* Director's Discretionary Time (DDT) observations (PI: De Pasquale). Meanwhile, *Swift* continued observing for several more days detecting a dim X-ray afterglow, which suggested that the steep decay had broken to a gentler slope. The *Chandra* observations of GRB 130831A took place on 2013 September 17 (T_0+16.6 d, or 1430 ks) and 2013 October 3 (T_0+33.1 d, or 2860 ks) with an exposure of 15 ks each. The location of GRB 130831A was imaged on the ACIS S3 chip in both observations. The ACIS data were processed using CIAO version 4.6 and version 4.5.9 of the Calibration Database (Fruscione et al. 2006) using standard tools. We filtered the events for grades 0, 2, 3, 4, and 6 and energy from 0.5–8 keV. We extracted the source counts within a 1.5 arcsec radius region centred on the best known position of the GRB, yielding 8 and 1 counts in the two observations, respectively. The first epoch yielded a detection with a significance of 5.4σ determined using the method described in Kraft et al. (1991). The second epoch was only $\sim1\sigma$ above background, thus it should not be regarded as a real detection.

2.2 Optical observations

Here, we describe how we collected, reduced and calibrated the ultraviolet, optical and infrared photometry of GRB 130831A. All magnitudes have been calibrated to the Vega system. The full set of photometric measurements is provided in an online table; a sample is shown in Table 3.

2.2.1 UVOT

Swift/UVOT (Roming et al. 2005) began observing the field of GRB 130831A 114 s after the trigger (Hagen et al., GCN Circular 15139) and started settled observations 191 s after the trigger, with a finding chart exposure in the *u* band. The afterglow was detected in all seven UVOT filters. Observations were taken in both imaging

Table 3. Photometry of the afterglow of GRB 130831A. All magnitudes are in the Vega system. The full table is available online.

$t - t_0$ (s)	Exposure time (s)	mag	Filter	Telescope
484	10	$14.86^{+0.09}_{-0.08}$	$uvw2$	UVOT
633	10	$14.03^{+0.06}_{-0.05}$	$uvw2$	UVOT
783	10	13.67 ± 0.05	$uvw2$	UVOT
10 346	450	$17.53^{+0.05}_{-0.04}$	$uvw2$	UVOT
43 951	2844	$19.44^{+0.15}_{-0.13}$	$uvw2$	UVOT
123 835	3414	>21.27	$uvw2$	UVOT
...	...	...	...	...

and event modes. Before extracting count rates from the event lists, the astrometry was refined following the method described in Oates et al. (2009). The source counts were extracted initially using a source region of 5 arcsec radius. When the count rate dropped to below 0.5 counts s^{-1} we then used a source region of 3 arcsec radius. In order to be consistent with the UVOT calibration, these count rates were then corrected to 5 arcsec using the curve of growth contained in the calibration files. Background counts were extracted using a circular region of radius 20 arcsec from a blank area of sky situated near to the source position. The count rates were obtained from the event and image lists using the *Swift* tools UVOTEVTLC and UVOTSOURCE, respectively. They were converted to magnitudes using the UVOT photometric zero-points (Breeveld et al. 2011). The analysis pipeline used version 20130118 of the UVOT Calibration Database.

2.2.2 RATIR

The Reionization And Transients InfraRed camera (RATIR; Butler et al. 2012) observed GRB 130831A over a period of 7 h, beginning

15.8 h after the *Swift* trigger, with follow-up observations on six nights over the next month. RATIR is mounted on the 1.5-metre Harold L. Johnson telescope of the Observatorio Astronomico Nacional on Sierra San Pedro Martir in Baja California (Mexico). This facility, which became fully operational in 2012 December, conducts autonomous observations (Klein et al. 2012; Watson et al. 2012) of its targets in the six photometric bands r', i', z', Y, J and H simultaneously. RATIR captured 80 s exposure frames in $r'i'$ and 67 s exposure frames in $z'YJH$ due to additional overhead. We applied their standard image reduction pipeline with twilight flat division and bias subtraction routines written in PYTHON and using astrometry.net (Lang et al. 2010) for image alignment and SWARP (Bertin 2010) for image co-addition. Aperture photometry was calculated using SExtractor (Bertin & Arnouts 1996).

2.2.3 NOT and LT

The 2.5 m Nordic Optical Telescope (NOT) and the 2 m Liverpool Telescope (LT), located at Roque de los Muchachos Observatory, La Palma in the Canary Islands (Spain), obtained three epochs of photometry presented in this paper: 2013 September 1 (*r* and *i*), 2013 September 3 (*i*), 2014 January 5 (*i*). Several additional epochs of *griz* NOT and LT photometry were obtained as part of a campaign to observe SN 2013 fu, which are presented in Cano et al. (2014). Image reduction of the *r* and *i* photometric data was performed using standard techniques in IRAF:[3] bias combine, bias-subtract, flat-field co-add, flat-field normalize, flat-field divide, align and co-add (Tody 1986, 1993). The optical data were calibrated using Sloan Digital Sky Survey (SDSS; Ahn, Alendandroff & Allende-Prieto 2012) stars in the GRB field, and converted into Vega magnitudes.

2.2.4 Skynet

Skynet (Reichart et al. 2005) obtained images of the field of GRB 130831A on 2013 August 31 with four 17 arcsec telescopes of the Panchromatic Robotic Optical Monitoring and Polarimetry Telescope (PROMPT) array at Siding Spring Observatory, New South Wales, Australia. Further observations were taken on September 1, this time observing also with the four 16 arcsec telescopes of the PROMPT array at the Cerro Tololo Inter-American Observatory, Chile and the 41 arcsec telescope at Yerkes Observatory, Wisconsin, USA. Beginning at 13:39 UT ($T–T_0 = 35.5$ min), exposures ranging from 60 to 180 s were obtained in the *BVRI* (PROMPT), and *g'r'i'* (Yerkes) bands. Bias subtraction and flat-fielding were performed by Skynet's automated pipeline. Post-processing occurred in Skynet's guided analysis pipeline, using both custom algorithms and ones based on IRAF. Differential aperture photometry was performed on single and stacked images, with effective exposure times from 60 s to 2.7 h. Photometry was calibrated against the catalogued *BVg'r'i'* magnitudes of six APASS[4] DR7 stars in the field (Henden & Munari 2014). The calibrations for *RI* magnitudes were derived using transformations obtained from prior observations of Landoldt stars (Henden, private communication).

2.2.5 IKI network for transients

The field of GRB 130831A was observed by several facilities of the follow-up network organized by the Space Research Institute (IKI) of Moscow, where observations of GRBs are planned and data reduction is carried out. We detail the observations of GRB 130831A of the individual observatories below.

The International Scientific Optical-Observation Network (ISON; Molotov et al. 2008; Pozanenko et al. 2013) started observing on 2013 August 31 at 13:14:32 UT, i.e. ∼10 min after the trigger, with the 0.65-m telescope SANTEL-650 (Volnova et al. 2013a) of ISON-Ussuriysk observatory. 30 unfiltered images, each with 120 s exposure, were taken. The 50-cm telescope VT-50 of ISON-Ussuriysk observatory started to observe at 13:26:10 UT, 22 min after the trigger, taking 384 unfiltered images with exposures of 30 s in two epochs with a gap of about 1.8 h (Volnova et al. 2013a). Starting at 19:12:30 UT during the first day, the 40-cm SANkovich-TELescope (SANTEL) -400AN of ISON-Kislovodsk observatory took 34 frames with exposures between 60 and 120 s (Volnova et al. 2013b).

The Astronomicheskii Zerkalnyi Telescope – 8 (AZT-8) 0.7-m telescope of Gissar (Tajikistan) observatory took 57 frames in *R* band with 60 s exposure time each starting at 17:47:54 UT.

The AZT-8 0.7-m telescope of the Chuguev Observational Station (Institute of Astronomy, Kharkiv National University) observed the afterglow in *R* filter starting on September 1 at 19:37:49 UT (Volnova et al. 2013c).

The optical afterglow was also observed by the 1.5-m telescope AZT-22 of Maidanak observatory (Uzbekistan) on 2013 September 1, 2, 4, 5, 7–11, 15, 16, 22, 27, and 29. Every observational night, frames were taken in the *R* filter with an exposure time of 600 s each. On September 1, we also took several frames in the *B*, *V* and *I* bands with the same exposure, and on September 2 we obtained additional observations in the *B* filter.

Most of the data obtained by Maidanak are presented in Cano et al. (2014) and used to study SN 2013 fu; in this article, we use the early data which were not contaminated by the supernova (SN) emission (see Section 3.3).

Observations were also taken with the 1.6-m telescope AZT-33IK of Sayan observatory (Mondy, Russia) on September 3, 4, and October 10, 11 and 14, taking several frames in the *R* band with an exposure of 60 s each. The optical afterglow was also imaged with the 2.6-m Shajn telescope of the Crimean Astrophysical Observatory on September 5, taking several frames in the *R* band with an exposure of 120 s each.

All data obtained by the facilities indicated above were processed with the same initial reduction including dark frame subtraction and flat-fielding, and using the IRAF packages APPHOT and DAOPHOT. For the photometric calibrations, we used four stars from the SDSS, indicated in Table 4. The *ugriz* magnitudes of the reference stars were transformed to the *BVRI* photometric system using the transformation equations attributed to Robert Lupton in the SDSS online documentation.[5]

2.2.6 GTC

The 10.4 m Gran Telescopio Canarias (GTC; Canary Island, Spain), equipped with the Optical System for Imaging and Low-Intermediate Resolution Imaging Spectroscopy (OSIRIS)

---

[3] IRAF is distributed by the National Optical Astronomy Observatory, which is operated by the Association of Universities for Research in Astronomy, Inc., under cooperative agreement with the National Science Foundation.
[4] http://www.aavso.org/apass

[5] www.sdss.org/DR7/algorithms/sdssUBVRITransform.html/Lupton2005

Table 4. Calibration stars which were used for the optical telescopes. RATIR used a much longer list of calibration stars, but we list only those in common with other instruments.

Catalogue	RA	Dec.	Telescopes
APASS	358.594 169	+29.341 196	Skynet RATIR
APASS	358.660 796	+29.429 860	Skynet RATIR
APASS	358.548 308	+29.427 729	Skynet RATIR
SDSS	358.682 125	+29.427 583	IKI RATIR
SDSS	358.660 833	+29.429 806	IKI
SDSS	358.598 500	+29.414 667	IKI RATIR
SDSS	358.643 042	+29.454 639	IKI RATIR
SDSS	358.635 21	+29.428 02	NOT, LT, RATIR
SDSS	358.632 96	+29.426 55	NOT, LT, RATIR
SDSS	358.621 88	+29.423 42	NOT, LT, RATIR
SDSS	358.639 86	+29.418 82	NOT, LT, RATIR
SDSS	358.647 47	+29.416 95	NOT, LT, RATIR

Table 5. Flux densities corresponding to zero magnitudes used in the conversion of magnitudes to flux densities for the light curves shown in Fig. 2.

Filter	Flux (Jy)
ISON unfiltered	2786
UVOT u	1445
UVOT $UVW1$	888
UVOT $UVM2$	769
UVOT $UVW2$	735
Skynet B	4127
Skynet V	3690
Skynet R	3103
Skynet I	2431
Skynet g'	363
RATIR r'	3147
RATIR i'	2590
RATIR Z	2211
RATIR Y	2040
RATIR J	1564
RATIR H	1007

instrument (Cepa et al. 2000), performed deep r'-band imaging of the GRB field 13330 ks after the trigger (2014 February 1), in order to obtain photometry for the host galaxy. Nine 60 s images were acquired in 2×2 binning, providing a pixel scale of 0.25 arcsec pixel^{-1}. The images were dark-subtracted and flat-fielded using custom IRAF routines. Aperture photometry was performed using DAOPHOT tasks as implemented in IRAF. Photometric calibration was based on SDSS standard stars present in the OSIRIS unvignetted field of view (7.8 arcmin $\times$ 7.8 arcmin).

2.2.7 Results from other facilities

In this subsection, we describe results obtained by other teams, not involved in our work. None the less, we will use their results in the next sections.

Konus-Wind Observations. GRB 130831A was observed by *Konus-Wind* onboard the *WIND* spacecraft. Golenetskii et al. (2013) found that this burst had a duration of 35 s; it was detected up to ~6 MeV. In addition, the spectrum is relatively soft; it can be fitted between 20 keV and 15 MeV with the Band model (Band et al. 1993), yielding a low-energy spectral index $\beta_1 = -0.61 \pm 0.06$, a high-energy spectral index $\beta_2 = -2.3 \pm 0.3$ and peak energy $E_p = 55 \pm 4$ keV. The fluence between 20 keV and 10 MeV is $(7.6 \pm 0.4) \times 10^{-6}$ erg cm^{-2} (90 per cent CL). We use the results of the *Konus-Wind* data analysis presented in Golenetskii et al. (2013), which spans a much wider spectral range than the BAT data, to derive the energetics of this burst. Thus, they are better suited to assess the energy emitted by the burst without using extrapolation. Using a cosmological k-correction (Bloom, Frail & Sari 2001) and the redshift $z = 0.479$ of this burst (Cucchiara & Perley 2013), we derive 1–10 000 keV rest-frame energetics of $E_\gamma = 1.06 \times 10^{52}$ erg. This burst follows the Amati relation (Amati 2006; Amati, Frontera & Guidorzi 2009; see also Cano et al. 2014, their fig. 12).

Radio. GRB 130831A field was also observed by the Jansky Very Large Array (EVLA) and Combined Array for Research in Millimeter Astronomy (CARMA; Zauderer, Laskar & Berger 2013). According to the analysis reported by Laskar, Zauderer & Berger (2013), no significant radio emission was detected: the 3σ upper limits are 38 μJy and 71 μJy at 5.8 and 21.8 GHz, respectively, at 0.64 d after the trigger. Similarly, CARMA obtained a 3σ upper limit of 780 μJy 0.76 d after the trigger (Zauderer et al. 2013).

2.2.8 Building the UVOIR light curves

In the subsections above, we summarized the observations of the optical instruments and how the data produced by each one were reduced. We shall now describe how we combined these different data sets into a homogeneous set of flux light curves. Magnitudes were translated to fluxes using the zero-magnitude flux densities listed in Table 5. Our overall approach has been that when data have been obtained from multiple observatories in the same (or almost the same) band, we scale all the data to match the data set which provided the largest number of measurements in that band. The largest set of measurements in r' and i' come from RATIR. We normalized the NOT and LT r' and i' data points to RATIR using the calibration stars common to the two data sets (see Table 4). The comparison of the calibration stars led us to scale the flux from the NOT r'-band data point by a factor of 0.99 and, based on the scatter between the NOT and RATIR measurements of the calibration stars we added a systematic error of 2 per cent to the errors on the NOT fluxes. The NOT and LT i'-band flux was scaled by a factor of 1.01 and a systematic error of 1 per cent was added. The Skynet Yerkes r' and i' data were matched to RATIR using the common reference stars listed in Table 4. The r' and i' fluxes from Skynet were scaled by factors of 0.94 and 0.91, respectively, and systematics of 3 per cent (r') and 2 per cent (i') were added to the uncertainties on the Skynet fluxes.

The largest set of measurements in B, V, R and I come from the Skynet PROMPT observations. To incorporate the UVOT v and b data into the V and B light curves, we first transformed the UVOT magnitudes of the GRB afterglow and the Skynet calibration stars into Johnson magnitudes using the appropriate colour transformations in Poole et al. (2008), before translating to flux densities. The UVOT and Skynet photometry of the Skynet calibration stars (see Table 4) were then compared to determine the appropriate scaling factors and systematic errors for UVOT. The UVOT V and B fluxes were scaled by factors of 1.13 and 1.07, respectively, and systematic errors of 9 and 6 per cent were added, respectively, to their flux uncertainties.

Based on the photometry of the calibration stars in common between the Maidanak and Skynet PROMPT observations (see Table 4) in the B, V and I bands, we scaled the Maidanak B, V

and *I* fluxes by factors of 1.01, 1.01 and 1.06, respectively, and added systematic errors of 10, 5 and 7 per cent. For the *R*-band data from the IKI Gissar, Maidanak, Chuguev and Sayan observatories, the calibration stars in common with Skynet suggested a scaling factor of 1.01 for these data and a 6 per cent systematic error, but the resulting GRB *R*-band light-curve from these observatories appeared to be systematically lower than that obtained from Skynet. A power-law fit to the *R*-band flux light curve derived from IKI observations between 15 and 100 ks, performed simultaneously with a power-law fit to the Skynet *R*-band data in the same time interval, and with the power-law slope tied between the two data sets, gives a best-fitting normalization for the IKI data which is 0.79 times that of the Skynet data. Therefore the IKI *R* fluxes were scaled by this factor before combining them with the Skynet PROMPT data.

3 RESULTS

3.1 Spectral analysis of X-ray data

The XRT spectral data (0.3–10 keV) were extracted in nine different temporal segments, with boundaries selected according to the different observing modes and breaks in the light-curve (see Table 2). Ancillary response files and exposure maps were created using the HEASOFT software for each segment, as well as appropriate response matrices from calibration data base. All the spectra were fitted using XSPEC v12.8.1 (Arnaud 1996) with an absorbed power-law model. Some indication of spectral evolution was found, with the spectral index trending from soft, during the first orbit, too hard from the second orbit onwards. Detailed results are shown in Table 1.

The X-ray spectrum between 9 and 132 ks, i.e. the end of the unusual late steep decay, can be modelled with a power law with Galactic absorption and intrinsic absorption at the redshift of the burst, $z = 0.479$. The Galactic absorption has been fixed to $N_H = 4.8 \times 10^{20}$ cm^{-2} (Kalberla et al. 2005). The best-fitting parameters are: spectral index $\beta_X = 0.77 \pm 0.07$, intrinsic $N_H(z = 0.479) = 6.8^{+3.3}_{-3.1} \times 10^{20}$ cm^{-2} which is consistent with 0 at 2.1σ CL.

To infer the late X-ray flux from *Chandra* measurements, we applied the following procedure. First, we corrected for the portion of the PSF excluded from the 1.5 arcsec radius aperture. Using the PC mode XRT spectral fit parameters (spectral index $\beta = 0.77$, intrinsic $N_H = 6.8 \times 10^{20}$ cm^{-2}), we derived 0.3–10 keV fluxes for the two epochs of $7.4 \pm 2.5 \times 10^{-15}$ erg cm^{-2} s^{-1} and $7.8^{+18.0}_{-6.5} \times 10^{-16}$ erg cm^{-2} s^{-1}, respectively. To derive the latter, we used the estimates on confidence limits for small numbers of events in astrophysical data (Gehrels 1986). The 3σ upper limit corresponding to the second *Chandra* observation is 7.4×10^{-15} erg cm^{-2} s^{-1}. Both XRT and *Chandra* fluxes are corrected for absorption. The results of the spectral analysis were used to compute the rate to flux conversion factors employed to build the flux light curve.

3.2 The X-ray light curve of GRB 130831A

The X-ray light curve is shown in Fig. 2. After an initial fast decay with slope $\alpha \simeq 6$ ending at $T_0 + 200$ s, there is an X-ray flare starting at about 500 s after the trigger and lasting at least up to the end of the first orbit at 900 s. The highest flux recorded was about 10^{-9} erg cm^{-2} s^{-1} at the beginning of XRT observations. When

GRB observations resumed, $\simeq 9$ ks after the trigger, the decay slope was slower than that at the very beginning of observations. This decay terminated at about $\simeq 100$ ks after the trigger, when the flux showed a surprisingly steep drop.

We fit the X-ray data (see Table 2) from the very beginning with the sum of an early power law, a broken power-law decay, a Gaussian flare superimposed on the second segment, and another, final power law. The first power law basically represents the tail of the prompt emission, probably due the curvature effect, which then gives way to a shallower decay usually attributed to a different emission mechanism (Zhang et al. 2006). When this second process ends as well, the flux falls quickly again. The late power law may represent emission powered by the FS mechanism, which can emerge once the emission from the previous process is over. The fit is acceptable, yielding $\chi^2/\text{dof} = 50.7/48$. We find a decay slope $\alpha_{X,2} = 0.8$ between 0.3 and 98 ks. Such a slope is intermediate between the typical shallow decay phase ~ 0.3 and the 'normal' decay phase ~ 1.2 seen in a wide sample of GRB afterglows (see Evans et al. 2009). We can still find a value of 0.8, however, in the distributions of decay indices of both phases. After the break at 98 ks, the best-fitting temporal slope is $\alpha_{X,3} = 5.9^{+1.0}_{-0.4}$, much faster than is usually observed in late X-ray afterglows, even in the case of a jet break, when $\alpha \sim 2$–3 (Sari, Piran & Halpern 1999; Racusin et al. 2009). This steep drop suggests that the X-ray afterglow might have been, until then, produced by some internal dissipation mechanism rather than the typical FS emission. With this fit model, the late power-law component has a decay slope $\alpha_{X,4} = 0.90^{+0.11}_{-0.05}$. We note that this decay slope of the X-ray flux after ~ 200 ks is steeper than the decay slope during the shallow decay phase. If the late X-ray flux were FS emission, it might have begun hundreds or even thousands of seconds after the trigger. However, the fitted model above does not include this possibility, and it may yield late power-law component slopes flatter than the real ones in order not to over-predict the flux at very early epochs. To better investigate the late emission, we use a different time interval. If we fit the X-ray data points from 100 ks onwards with a simple power-law model, we obtain a poor fit, $\chi^2/\text{dof} = 17.8/5$. The best-fitting decay slope is $\alpha_{X,3} = 4.6^{+0.5}_{-0.4}$. However, if we fit the same data points with a power-law + power-law model, we obtain a much better fit, with $\chi^2/\text{dof} = 2.4/3$. This model yields a decay slope for the first power law of $\alpha_{X,3} = 6.8^{+2.0}_{-1.5}$, with a 3σ lower limit (with $\Delta\chi^2 = 9$) of $\alpha_{X,3} = 3.9$. Such a value, though, is still too steep for the FS model, see above. The best-fitting value for the late power-law component is $\alpha_{X,4} = 1.11^{+0.22}_{-0.29}$, while its flux at 2 d (173 ks) after the trigger is $6.08^{+2.31}_{-2.77} \times 10^{-14}$ erg cm^{-2} s^{-1}.

An analysis with the *F*-test suggests that the two-power-law model is not necessary, because the probability of an improvement by chance is 4 per cent, which is not negligible. However, if we adopted the simple power-law model with the steep decay slope $\alpha = 4.6$ after 100 ks, then the flux at the time of the first *Chandra* observation would be $\simeq 5 \times 10^{-17}$ erg cm^{-2} s^{-1}. Such extremely low flux corresponds to less than 0.1 counts with a ACIS-S 15 ks observation; thus our first *Chandra* observation would most likely yield 0 counts. We can place a 99.5 per cent CL upper limit of 5.3 counts, according to Gehrels (1986). This prediction, however, is in disagreement with the fact that the observation actually produced eight counts. According to Kraft et al. (1991), these eight counts represent a 5.4σ detection. We therefore conclude that the X-ray afterglow decay has become much shallower at late epochs, and we will adopt the results of the fit of the two power-law model after 100 ks.

Table 6. Results of the temporal analysis of the optical emission of GRB 130831A between 3.5 and 15 ks (upper part) and 15 ks and 13 Ms (lower part). Time is expressed in ks, while the constant flux is in μJy. Since the host galaxy constant flux is not important during the first fit, which does not extend up to late times anyway, we have omitted it.

Filter	α_1	$t_{b,1}$ (ks)	α_2	Const (μJy)	$\chi^2/$dof
No filter	$0.06^{+0.19}_{-0.20}$	$4.79^{+0.16}_{-0.17}$	1.62 ± 0.07	–	86/53
B	0.42 ± 0.08	4.90 ± 0.08	1.45 ± 0.03	–	81/49
V	0.86 ± 0.03	6.47 ± 0.10	1.65 ± 0.03	–	160/57
R	$0.64^{+0.04}_{-0.06}$	$5.56^{+0.11}_{-0.16}$	1.56 ± 0.02	–	232/57
I	0.92 ± 0.03	$6.99^{+0.17}_{-0.19}$	$1.82^{+0.05}_{-0.06}$	–	119/50
R	1.60 ± 0.03	–	–	0.81 ± 0.14	9.4/10
r'	1.49 ± 0.06	–	–	0.96 ± 0.11	30.7/14
i'	1.64 ± 0.07	–	–	0.73 ± 0.08	29.2/15

3.3 Optical light curve of GRB 130831A

The combined optical light curves in Fig. 2 show an initial short plateau, which lasts until ∼500 s, followed by a steep rise and a peak at ≃800 s. This optical flare is basically concurrent with the X-ray flare. Following the flare, there is another plateau that in turn gives way to a steeper decay at ≃5000 s. In this phase, fitting the optical light curves with simple models such as a broken power law does not provide a statistically acceptable fit. For example, the best fit of B-band data between 3.5 and 15 ks with a broken power law yields an early decay slope of $\alpha_1 = 0.42 \pm 0.08$, break time $t_{break} = 4.90 \pm 0.08$ ks, and post-break slope $\alpha_2 = 1.45 \pm 0.03$ with $\chi^2/$dof = 81/49. Fitting the other light curves in this interval yields similar results. We none the less plot the best-fitting curves in Fig. 2, as an indication for the behaviour of the optical afterglow, and report the results of fitting the light curves in the interval between 3.5 and 15 ks in Table 6. Such high χ^2 are due to some 'wiggles' of the densely sampled light curves in this phase, which has been seen in other GRBs (e.g. Matheson et al. 2003; Swenson et al. 2013). The post-plateau decay is moderately steep and does not seem to change its slope at the epoch of the X-ray drop. However, about ∼5 d after the trigger, the optical emission starts to rise due to light coming from SN 2013 fu, the SN associated with GRB 130831A (Klose et al. 2013; Cano et al. 2014). Given the complication of considering the SN flux, we have excluded all data points that had a >10 per cent contribution from the SN, basically those after ∼230 ks and before ∼6000 ks. The SN contribution at these epochs have been estimated using the SN 1998bw template program presented in Cano (2013).

In addition, we have observations at $T - T_0 > 100$ d in r' and i' filters, taken with GTC and LT (see Sections 2.2.3 and 2.2.6). These late-time data do not suffer significant contamination from the SN and the afterglow, which have faded away. They correspond to the magnitude of the host galaxy, and have been used to determine the optical afterglow behaviour (see below). Vega magnitudes of the host galaxy are $r' = 23.75 \pm 0.11$, $i' = 23.83 \pm 0.10$. Assuming the conversions from Jordi, Grebel & Ammon (2006, their table 1), we find a Vega magnitude $R = 23.84 \pm 0.15$. Spectral observation taken at the Gemini North Observatory revealed that GRB 130831A occurred at redshift of $z = 0.479$ (Cucchiara et al. 2013). For such a redshift, the magnitude of the host corresponds to a luminosity $L \simeq 0.04 L_\star$ in the B band (Hjorth et al. 2012).

We know the host contribution in R, r' and i' only, from our late-time GTC and LT images. We fitted the light curves in these filters with the same model, namely a power-law $F \propto t^{-\alpha}$ plus constant, from 15 ks up to 100 d after the trigger. We ignored the data before 15 ks because they would lead to a very bad fit,

as we previously noted (see above). The best-fitting decay slopes and χ^2 are $\alpha_R = 1.60 \pm 0.03$, $\chi^2/$dof = 9.4/10; $\alpha_{r'} = 1.49 \pm 0.06$, $\chi^2/$dof = 30.7/14; and $\alpha_{i'} = 1.64 \pm 0.07$, $\chi^2/$dof = 29.2/15 (see Table 6). These fits are statistically acceptable and consistent within 2σ. We find that the weighted mean is $\alpha_{opt} = 1.59 \pm 0.03$. The decay slopes of the flux in other filters are consistent with this value within 3σ as well. We note that Cano et al. (2014), in their analysis of the afterglow light curves, find that the optical decay slope is $\alpha = 1.63 \pm 0.02$, consistent with our analysis. We remark upon the fact that we can fit the optical light curves with an uninterrupted power law, even across the X-ray break. This feature strongly suggests that optical and X-ray emission (at least part of it) have different origins.

3.4 Spectral energy distributions

To test the hypothesis that the late emission is entirely due to FS, we built an SED with the available UVOIR + X-ray data at 2 d after the trigger (173 ks).

First, we calculated the count rates at 2 d. We used the data between 15 and 100 ks, since no colour evolution was detected in the UV to the near-IR, and the count rate in all light curves could be fitted as a power law with a common decay index $\alpha = 1.59$ between these two epochs. The UVOT data were translated to XSPEC-compatible files using the standard FTOOL UVOT2PHA. Then, we adjusted the count rates of these files to the values determined by fitting the light curves. Each of the ground-based optical and near-IR photometric data points were imported into XSPEC using bespoke software, as follows. Each photometric data point was recorded as a single-channel spectral file containing a count rate and count rate uncertainty, with a corresponding response file. To produce the response files, the responsivity of the filter/telescope combination as a function of wavelength was converted to a normalized effective area as a function of energy. As for the X-ray, we first determined the light-curve count rate at 2 d, fit_{CR}. We then determined a new exposure time t_{newexp} for which $spec_{CR}/t_{newexp} = fit_{CR}$, where $spec_{CR}$ is the count rate of the source after background subtraction. We then imported the source and background XRT spectral files with the changed exposure times into XSPEC. To build the SED, we used the XRT data after the steep decay slope, but did not use the *Chandra* data because XRT and *Chandra* fluxes would have to be renormalized to the same value and XRT has more counts.

We fitted the optical and X-ray data with XSPEC (Arnaud et al. 1996). We adopted a simple power-law model with two absorbers and two *zdust* components, one at $z = 0$ and another one at $z = 0.479$, i.e. the redshift of the burst (Cucchiara et al. 2013). The values of the
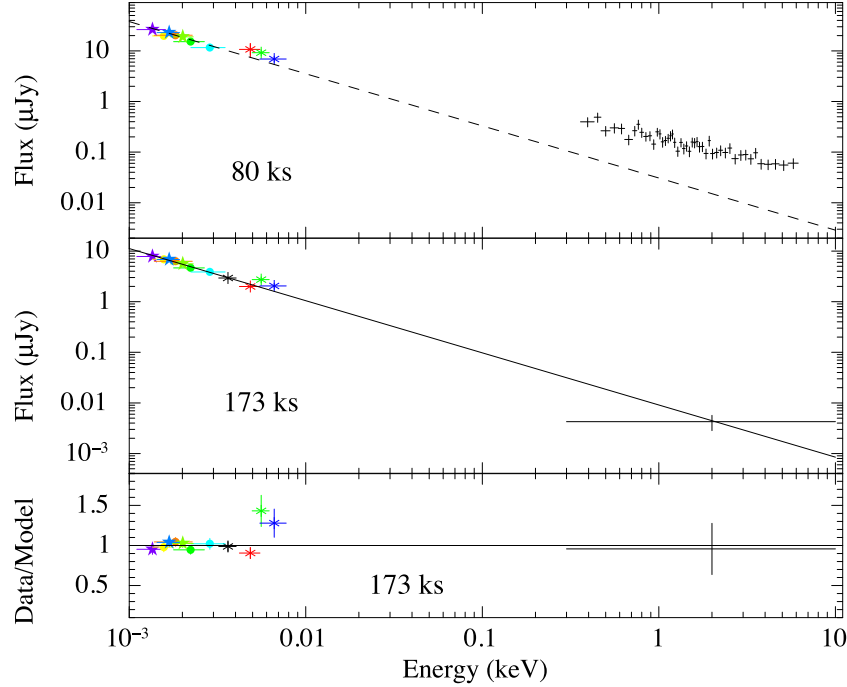
Figure 3. SEDs of GRB 130831A at 80 ks (top) and 173 ks (2 d) after the trigger (bottom). At 173 ks, we plot on the SED the best-fitting model, a simple power-law model with $\beta_{OX} = 1.03$. We rescaled this best-fitting model, multiplying the normalization constant by $(173/80)^{1.59}$, where 1.59 is the temporal decay slope, and we plot such an 'extrapolated model' with a dashed line on the 80 ks SED. Such an extrapolation predicts the optical but clearly underestimates the X-ray emission, which must be produced by a component not present at 173 ks. Each filter has the same colour in the plot.

Table 7. Best-fitting parameters obtained when fitting the 173 ks (2 d) SED with a single broken power-law and MW extinction law. We indicate the reddening in our Galaxy and that in the host at $z = 0.479$ separately. The absorption in our Galaxy ($z = 0$) and in the host of the GRB ($z = 0.479$) has been fixed to the best-fitting value of the X-ray data.

N_H at $z = 0$	N_H at $z = 0.479$ $\times 10^{22}$	$E(B - V)$ at $z = 0$ (mag)	$E(B - V)$ at $z = 0.479$ (mag)	β_{OX}	χ^2/dof
4.8×10^{20}	0.068	4.0×10^{-2}	$1.8 \pm 1.3 \times 10^{-2}$	$1.03^{+0.05}_{-0.04}$	12.7/9

absorbers are the same given in the X-ray data analysis Section 3.1. The Galactic reddening was fixed at $E(B - V) = 0.04$ mag according to the map of Schlegel, Finkbeiner & Davis (1998). As for the extinction at the redshift of the burst, we tried the Milky Way, Large and Small Magellanic Clouds (MW, LMC and SMC) extinction laws as in Pei (1992). We found that all of them yield acceptable and similar fitting results. However, the MW extinction law provides the best fit, so we have adopted the results of the fit with this law. The SED of GRB 130831A at 2 d is shown in Fig. 3. The best-fitting parameters are an index $\beta_{OX} = 1.03^{+0.05}_{-0.04}$ and a small or absent amount of extragalactic reddening $E(B - V) = 0.02 \pm 0.01$ mag (Cano et al. 2014, find a negligible rest-frame extinction as well); this fit yields χ^2/dof $= 12.7/9$. A broken power-law model does not significantly improve the fit, since it yields $\chi^2 = 12.4/8$ and the break energy is unconstrained. Moreover, fits with LMC and SMC extinction law result in a break energy above the X-ray band. All in all, we believe that a simple power-law model is adequate to describe the SED at this late epoch. Results of the fit of the 173 ks SED are shown in Table 7. There are only $\simeq 15$ counts collected by XRT after the fast drop, and to build the SED and obtain the quoted results we constructed a single X-ray data bin spanning from 0.3 to 10 keV. We were concerned that the use of such a wide bin might be not the optimum in the SED fitting process. There-

fore, we repeated the fit using standard χ^2 statistics with optical data and Cash statistics for the X-ray data, where the bins were constituted of single counts. We obtained very similar results. The fit with a simple power-law model yielded $\beta_{OX} = 1.03^{+0.05}_{-0.04}$, $E(B - V) = (1.9 \pm 1.3) \times 10^{-2}$ mag with total statistics of 23.4 and 26 dof. A fit with a broken power-law model was marginally better, yielding statistics of 22.2 with 25 dof, but the F-test indicates that the probability of an improvement by chance was high, with a probability of 25 per cent.

We also show that the same model does not apply to earlier data. Following the same procedure outlined above, we built an SED with UVOIR and X-ray data at 80 ks (Fig. 3), before the steep X-ray drop. Then, we changed the normalization of the 173 ks power-law fit, following a decay slope of $\alpha = 1.59$. We then plotted such a re-normalized power-law model with $\beta_{OX} = 1.03$ onto the 80 ks SED. We see that, while the optical emission is easily matched, the observed X-ray flux lies well above the model prediction. This finding is confirmed by the fact that if we fit the 80 ks SED with the same power-law model used for the 173 ks SED, we obtain a best-fitting spectral slope $\beta_{OX} = 0.76 \pm 0.01$. This is harder than the slope found at 2 d and inconsistent with it. This result confirms that the spectrum at 80 ks across the X-ray and optical bands is not consistent with the spectrum at 173 ks and lends credence to the

idea that there is an additional component in the X-ray band at early epochs.

4 DISCUSSION

4.1 Modelling of GRB 130831A and the efficiency of its 'central engine'.

We found that the X-ray light curve, after the steep drop at 100 ks, resumes a slower decay slope of $\alpha_{X,4} = 1.11^{+0.22}_{-0.29}$; such a decay slope is statistically consistent with the optical decay slope from 15 ks onwards, $\alpha_{opt} = 1.59 \pm 0.03$, at 2.1σ CL. The SED at 2 d (173 ks) after the trigger is adequately fit with a simple power-law model, in which the X-ray and the optical band lie on the same spectral segment. Values of the spectral and temporal indices seem to be typical of GRB late afterglow emission, and are easily explainable by the FS model.

The FS model predicts basic relations between spectral and decay indices (for a review, see Zhang et al. 2006), which depend on the type of expansion (spherical or jet) and the spectral regime, i.e. where the observing bands are located relative to the synchrotron peak frequency and cooling frequency, ν_m and ν_c respectively, and the density profile of the circumburst medium. We can use these closure relations to find the conditions that apply to the case at hand. We adopted α_{opt} as decay slope, since it is better constrained than the late X-ray decay index, and β_{OX} as the spectral slope. If the observing bands (both the X-ray and optical) were below ν_c and the medium had a constant density profile, we would have $\alpha - \frac{3}{2}\beta = 0$; this is in agreement with observations at 1σ. If the medium had a stellar wind profile, with density ρ decreasing with radius r as $\rho \propto r^{-2}$, then $\alpha - \frac{3}{2}\beta - 1/2 = 0$; this is ruled out at $\simeq 10\sigma$ level. If the observing frequency is above the cooling frequency, for both the constant medium and stellar wind profile cases the relation $\alpha - \frac{3}{2}\beta + 1/2 = 0$ should be satisfied; but this is rejected at $\simeq 10\sigma$. Finally, if the outflow is collimated and has decelerated enough so that the observer detects emission from the edges, the decay should become steeper ('jet break'). After the jet break, the relations to satisfy are $\alpha - 2\beta - 1 = 0$ and $\alpha - 2\beta = 0$ if the observing frequency is below or above ν_c. These relations are ruled out at 16σ and 5σ, respectively. The only relation of those above fulfilled within 1σ is that for the observing frequency below ν_c, constant density medium, and pre-jet break expansion.

In the context of the FS model, the flux produced by the afterglow depends on several factors, such as the kinetic energy E_K of the outflow, the fraction of energy given to radiating electrons ϵ_e and to the magnetic field ϵ_B, the density of the environment n, the slope of the power-law energy distribution of electrons p, the type of expansion and where the observing bands are located. It is possible to derive the kinetic energy through simple relations once the flux is known, but one has to make assumptions of the values of the other parameters.

Following Zhang et al. (2007), the flux density F_ν of the FS emission is given by

$$F_\nu(\nu_m < \nu < \nu_c) = 1600 D_{28}^{-2}(1+z)^{\frac{3+p}{4}} \epsilon_{B,-2}^{\frac{p+1}{4}} \epsilon_{e,-1}^{p-1}$$

$$\times E_{K,52}^{\frac{3+p}{4}} n^{1/2} t_d^{3/4(p-1)} f_p^{p-1} \left(\frac{\nu_{3.3 \times 10^{12}}}{\nu}\right)^{\frac{p-1}{2}} \mu Jy, \quad (1)$$

where f_p is a parameter depending on p, and D is the luminosity distance in cm. Subindices indicate normalized quantities, $Q_x = Q/10^x$ in cgs units. A spectral index $\beta_{OX} = 1.03$ for an observing frequency ν between ν_m and ν_c implies $p = 3.06$. Such a large value of p is

not very common; typically $p = 2.1$–2.5. However, $p = 3.06$ is still within two standard deviations from the centre of the distribution of this parameter, as implied from the analysis of more than 300 *Swift* GRBs (Curran et al. 2010), and we will adopt this value. As for the observing frequency, we take $\nu = 2.42 \times 10^{17}$ Hz, i.e. 1 keV. We convert the X-ray flux between 0.3 and 10 keV into a flux density of $\simeq 7 \times 10^{-3}$ μJy at this frequency.

From the equation above, we obtain

$$\epsilon_{B,-2}^{1.02}\epsilon_{e,-1}^{2.06} E_{K,52}^{1.52} n^{1/2} \simeq 2.0. \quad (2)$$

We infer $E_{K,52} = 11.8$ if we assume $\epsilon_{e,-1} = 2.7$, $\epsilon_{B,-2} = 0.2$, and $n = 10^{-3}$. These low values of ϵ_B and n are required to have ν_c well above the X-ray band 2 d after the trigger. A lower value of ϵ_B may imply significant Inverse Compton flux, which is usually not detected in GRBs. The low density is not totally unprecedented in GRB afterglow modelling, since it has already been found for events in constant density media (Panaitescu & Kumar 2002; Cenko et al. 2011, with radio observations) and stellar wind media (Cenko et al. 2011; Perley et al. 2014). On the other hand, a density *lower* than $\sim 10^{-3}$ is not usually expected in long GRBs, which occur next to, or within, dense star-forming regions. We also note that E_K has a weak dependence on n, so our inferred E_K would not be dramatically different if the value of this parameter were within one order of magnitude from what we use. As for $\epsilon_{e,-1}$, the value we have chosen is close to that of equipartition, and is obtained by modelling GRB afterglows (see aforementioned references). However, we now show that in our modelling we cannot have $\epsilon_{e,-1} \lesssim 2.5$. From equation (2), we have $E_K \propto \epsilon_e^{-4/3}$ roughly. FS theory predicts that $\nu_m \propto E_K^{1/2}\epsilon_e^2$ and $F_\nu(\nu_m) \propto E_K$, where $F_\nu(\nu_m)$ is the peak synchrotron flux reached at ν_m. For $\nu < \nu_m$, $F_\nu \propto \nu^{1/3}$; the flux below ν_m will therefore be $F(\nu) \propto \epsilon_e^{-16/9}$. For the values of the parameters quoted above, the radio flux at 22 and 5.8 GHz predicted 0.67 d after the trigger would be 56 and 36 μJy, respectively, below the upper limits determined by the VLA (Laskar et al. 2013). However, if $\epsilon_{e,-1}$ were less than 2.5 the predicted radio flux would instead be larger than the above limits. We note, though, that interstellar scintillation could suppress the observed radio flux as well. For the values of parameters we have constrained, the FS peak flux will be $\simeq 550$ μJy. Such a flux is quite typical for GRB FS peak; see Chandra & Frail (2012) and de Ugarte-Postigo et al. (2012). We can assume that our estimate on E_K is robust at least to an order of magnitude.

The modelling above enables us to determine the efficiency η of the conversion of the energy of the outflow into energy E_γ emitted in high-energy photons during the prompt emission. The efficiency is defined as $\eta = E_\gamma/(E_K + E_\gamma)$. Given $E_\gamma = 1.06 \times 10^{52}$ erg and the value of E_K constrained above, we find $\eta \simeq 0.07$. By means of both optical and X-ray data, we have thus measured the efficiency of the central engine of a GRB with a prolonged internal emission episode. The optical light curves were well sampled, and late *Chandra* observations constrained the X-ray flux light curve after the steep drop. Thus, we could establish with little doubt that the late emission was entirely consistent with the FS model. Zhang et al. (2007) and, more recently, Lü & Zhang (2014) carried out a similar task by using XRT light curves; such a study with X-ray data alone, especially without precise late measurements, may be more ambiguous.

An efficiency of $\eta \simeq 0.07$ is lower than that of those few GRBs that unambiguously show a plateau of 'internal origin' (see fig. 12 of Lü & Zhang 2014). The efficiency of GRB 130831A is more characteristic of those GRBs that have their afterglow emission entirely explained by the FS mechanism, but with the presence of energy injection into the ejecta perhaps powered by a magnetar.

Typically, GRBs with a plateau of internal origin have $\eta \sim 0.5$–1, while those explained by FS have a range of $\eta \sim 0.001$–0.1 with most clustering around $\eta = $ a few $\times\ 0.01$.

4.2 Origins of the X-ray radiation between the end of the prompt emission and up to the 100 ks drop.

4.2.1 Observations

The sudden drop in the X-ray flux at $\simeq 100$ ks, with a decay index $\alpha_{X,3} \simeq 7$, cannot be interpreted as FS emission. The steepest decay in this model is $\alpha = p$, where p is the index of the power-law energy distribution of radiating electrons, which occurs during a jet-break expansion phase. However, $p \simeq 7$ is not predicted at all on theoretical grounds (e.g. see Rieger, Bosch-Ramon & Duffy 2007); thus, it is very difficult to explain such a steep decay index at late times. Theoretically, an index as steep as $\alpha \sim 3$ can be achieved by taking into account relativistic effects in simulations (e.g. Granot 2006; van Eerten, Zhang & MacFadyen 2010) even if $p < 3$, but the value of the decay index reached in the case of GRB 130831A is greater than this prediction. Duffell & MacFadyen (2014) explored the possibility that the plateaux we see in GRB afterglows are produced by a jetted outflow before deceleration, followed by a steeper decay, which flags the Blandford & McKee deceleration of the ejecta. However, such a decay in their model does not reach a value as steep as $\alpha \sim 7$ detected in GRB 130831A between 100 and 200 ks.

By assuming that the steep decay is due to the curvature effect (Kumar & Panaitescu 2000; see also Uhm & Zhang 2014), we followed Liang et al. (2006) to test the internal origin of X-ray emission up to the steep break. We found that to satisfy the $\alpha \simeq \beta + 2$ condition of the curvature effect, the zero time T of this emission needs to be $\simeq 75$ ks after the trigger, slightly before the beginning of the flux drop. The very steep decay component therefore strongly suggests that the X-ray emission up to 100 ks is of internal origin, since T is allowed to occur at large time intervals from the initial prompt emission in this case (Liang et al. 2006; Zhang et al. 2006).

In a more general study of the curvature effect emission (Uhm & Zhang 2014), the emitting ejecta are assumed to accelerate or decelerate while producing the radiation. If the ejecta are accelerating, which may be the case for the magnetically dominated jet of the ICMART model (Zhang & Yan 2011), the decay index may temporarily reach a value of $\alpha \sim 7$ we observe even assuming T as the trigger of the prompt emission and $\beta \sim 1$. A magnetically dominated jet thus appears to be a reasonable solution for the GRB at hand.

However, whichever solution applies, one would always have to assume that the emission is produced inside the ejecta and not in the medium surrounding the explosion as in the case of the FS scenario. Finally, in the previous section we made it clear that the final part of the X-ray light curve, after the end of the steep decay, appears to be FS emission.

We conclude that the X-ray emission up to the 100 ks break is not produced by the external, circumburst medium energized by the FS, but it is instead of 'internal origin', generated directly within the explosion outflow. This component stops abruptly and the X-ray flux drops rapidly, until the FS emission in the X-ray band prevails. The optical emission is basically dominated by the FS mechanism (with the possible exception of the early flare; see Section 4.5). In the next sections, we shall discuss the possible origins of the high-energy emission between the end of the prompt emission and the fall of the X-ray flux at 100 ks.

4.2.2 A magnetar central engine

The nature of the X-ray afterglow and the nature of the central engine are two of the many open questions in the contemporary field of GRBs (see Zhang 2011 for a review), even more so because this GRB shows that we may be misinterpreting the behaviour of other X-ray light curves solely or primarily attributed to FS. For example, if we had not observed the steep drop at 100 ks for 130831A, we might have easily mistaken the relatively ordinary decay and spectral slopes as being produced by the standard FS-emission.

The core of the stellar progenitor of GRB 130831A may have collapsed into a magnetar (see for example Thompson et al. 2010). The rotational kinetic energy $E_{\rm rot}$ of such objects is

$$E_{\rm rot} = 3 \times 10^{52} \left(\frac{M}{1.4\ \rm M_\odot} \right) \left(\frac{R}{12\ \rm km} \right)^2 P_{\rm ms}^{-2}\ \rm erg, \qquad (3)$$

where M, R and P are the mass, radius and period in ms of the object, respectively. Assuming unitary values for the parameters above, $E_{\rm rot} \simeq 3 \times 10^{52}$ erg, which is enough to power the SN explosion and ultrarelativistic outflow. If the mass M is closer to the Tolman–Oppenheimer–Volkoff limit, which is thought to be slightly larger than $2\,{\rm M_\odot}$ (Antoniadis, Freire & Wex 2013), the parameter $E_{\rm rot}$ might be slightly different (Metzger et al. 2015).

In a simple scenario, the magnetar would initially tap into rotational energy and produce a very energetic outflow, likely roughly collimated into bi-polar jets. Such a wind would be produced through the process of dipole spin-down. The energy of the outflow is initially imparted to the stellar envelope, causing, or at least contributing to, the SN explosion. Moreover, the magnetar outflow may be long-lived, and produce radiation that we observe (see below). In this scenario, the luminosity L_0 of the magnetar could be roughly constant, even for a relatively long time-scale $T_{\rm em}$ (Zhang & Mészáros 2002), depending on physical parameters. After $T_{\rm em}$, or if the magnetar collapses into a black hole, the light curve would show a flux drop. This magnetar model is relevant for a few GRBs that show a plateau with approximately constant flux, with $\alpha \simeq 0$, followed by the steep slope segment (see cases studied by Liang et al. 2007; Bernardini et al. 2014; Cano et al. 2014; Lü & Zhang 2014; Lü, Zhang & Lei 2015). However, the early decay slope of 130831A is $\alpha_X \simeq 0.8$, which is in contrast to the aforementioned cases, and requires a more complicated model to explain our observations.

4.2.3 A Magnetar with decaying magnetic field

In the simple spin-down calculation above, one assumes that the magnetic field B is constant and independent of the period of the magnetar P. Metzger et al. (2011), however, assume that B is linked to P, taking into account that the magnetic field is generated from the energy available in differential rotation. They thus estimate

$$B = 10^{16} R_6^{-1/2} P_{-3}^{-1}\ \rm G. \qquad (4)$$

Under this assumption, B decreases with increasing P, i.e. with increasing time since the explosion. In such conditions, the jet luminosity L is not constant. As shown in figs 2 and 5 of Metzger et al. (2011), L decreases with time, scaling approximately as $L \propto t^{-1}$ from 100–1000 s to tens of ks after the collapse for reasonable values of parameters at the beginning of the spin-down, such as $B_0 \simeq 10^{15}$ G and $P_0 = 1$–2 ms. The predicted luminosity of the jet seems to be in the right range to explain the X-ray emission of GRB 130831A during the slow decay phase, too. For the values quoted above, Metzger et al. (2011) predict a few $\times\ 10^{46}$ erg s^{-1} at 10 ks; at the same epoch, GRB 130831A had a luminosity of $\sim 10^{46}$ erg s^{-1}.

We note that a jet luminosity L_{jet} does not convert immediately into X-ray luminosity L_X; one has to take into account that the radiation mechanism will have a certain efficiency. Moreover, we have not yet considered that GRB emission is beamed. We can write

$$L_X = \eta_X f_{\text{b,x}}^{-1} L_{\text{jet}}, \tag{5}$$

where η_X and $f_{\text{b,x}}$ are the efficiency in converting the jet luminosity into X-ray radiation and the correction for the beaming, respectively.

According to Metzger et al. (2011), at late epochs ($>$100–1000 s after the collapse), the magnetar outflow is highly relativistic and Poynting-flux dominated; in such conditions, internal shocks and reconnections within the jet itself are not possible. Forced reconnection, however, can occur at large radii, when the outflow collides with the circumburst medium and/or the previous ejecta, and convert the jet energy into X-ray emission. Assuming that the efficiency of this process is similar to the one which generates the prompt emission, and the correction for beaming is 10 times lower than that during the prompt emission, Metzger et al. (2011) find that they can explain the observed L_X and plateau durations of several GRBs similar to GRB 130831A.

The newly born magnetar may also provide a large energy input in the exploding progenitor, powering an energetic and luminous SN explosion. This is in agreement with observations of Cano et al. (2014), who find a kinetic energy for the (non-relativistic) ejecta of SN 2013 fu of $E_{\text{SN}} = 1.9 \times 10^{52}$ erg and a peak absolute magnitude $M_V = -19.3$. We note that Greiner et al. (2015) found $E_{\text{SN}} \simeq 10^{52}$ erg for SN2011 kl, a very bright SN associated with GRB 111209A, whose properties can be explained by the energy injection of a newly born magnetar. In addition, the energetics of SN 2013 fu is quite typical of other SNe associated with GRBs (Cano et al. 2015).

As for the abrupt end of the X-ray emission of 'internal origin', with a very steep slope, we may attribute it to the delayed collapse of the magnetar into a black hole (Vietri & Stella 1998; Lyons et al. 2010; Rowlinson et al. 2013). Once the magnetar has lost much of its rotational energy to power the jet, the weakened centrifugal forces may not be able to avoid the collapse. The time-scale of such event, for an NS mass of $\sim$2 M$_\odot$, initial period of $\sim$2 $\times$ 10^{-3} s and magnetic field of 10^{15} Gauss would be $\sim$6 $\times$ 10^4 s (Vietri & Stella 1998, their equation 1), comparable to the epoch of the steep drop in the X-ray light curve of GRB 130831A. Such a collapse should be relatively quick, and rapidly stop energy emission from the central object. If a magnetar collapsing into a black hole is the right model, GRB 130831A might be a candidate for the production of fast radio bursts (FRBs), as described in Zhang (2014), as thus a target for observational campaigns in radio aimed at understanding the origin of FRBs.

4.2.4 A black hole with a fall-back accretion disc

Another possibility we consider is that the central engine of this GRB could be a stellar black hole with a fall-back accretion disc (Kumar et al. 2008). Basically, in the SN explosion associated with the GRB, the innermost part of the star collapses into a black hole. A continued fall-back of matter – directly from the progenitor envelope or from SN ejecta that failed to reach escape velocity – occurs at the centre. Some of this material does not accrete directly on to the black hole, but creates an accretion disc around it. Depending on the fall-back rate and the accretion time t_{acc} on to the black hole, the material of this disc can power relativistic ejecta from the black hole for a long time, which may produce both the prompt emission and a long-lived, slowly decaying X-ray flux.

For the latter, Kumar et al. (2008) envisage a few possibilities. One is that the accreting disc has a low viscosity. It will thus take a long time, of the order of $\sim$10^4–10^5 s, for the all the disc material to accrete on to the black hole and power the jet. This model explains a long-lived plateau, but it predicts a flux decay with slope $\alpha \simeq 1.3$ at the end of this phase, which is not observed in GRB 130831A and other GRBs with similar features.

Another possibility is that the disc has high viscosity. Then t_{acc} is much less than the fall-back time, and the emission basically traces the rate of the matter falling back on to the accretion disc. However, such a scenario cannot explain why the fall-back rate is less steep than expected: on theoretical grounds, we expect a fall-back rate to vary as $t^{-5/3}$ (Chevalier 1989). Secondly, the plateau slope and the sudden cut-off can be explained only by a particular density and angular momentum profile of the matter of the progenitor. A luminosity that evolves close to t^{-1}, as in the case of GRB 130831A, might be explained if the density profile of the stellar envelope has a profile of approximately r^{-3}, where r is the radius from the centre of the star. A steep drop at the end of the plateau might be achieved if the material of the stellar envelope, which is the last to be accreted, has a relatively small angular momentum: this will cause the matter to fall rapidly on to the black hole and shut off the emission. Such a peculiar configuration, however, seems somewhat contrived and at odds with models of stellar progenitors (e.g. Woosley 2012). Moreover, to support accretion for $\sim$10^5 s, the disc should be unusually large and massive, leaving little mass for ejecta. Cano et al. (2014) find instead that the SN 2013 fu, associated with GRB 130831A, has an ejecta mass of $M_{\text{ej}} \approx 4.7$ M$_\odot$, which is typical of other GRB-SNe (e.g. Cano 2013).

For the model discussed, the jet luminosity is expected to be in the range of 10^{45} erg s^{-1} at the end of the plateau, which is similar to the X-ray luminosity of the GRB 130831A afterglow at the end of the shallow decline phase.

4.2.5 A binary origin

Barkov & Komissarov (2010) conceive another scenario in which a black hole might power a GRB and long-lived outflow (see also Komissarov & Barkov, 2009). If a compact object and a Wolf–Rayet (WR) star form a very close binary, such a system can go through a common envelope phase in which the compact object spirals in and can accrete the matter of the companion. The common envelope matter will have very high angular momentum and can take a long time to accrete. According to Barkov & Kommisarov, the accretion time-scale of such a system is

$$t_{\text{d}} \simeq 8000 \left(\frac{\alpha}{0.01}\right)^{-1} \left(\frac{R_{\text{s}}}{R_\odot}\right)^{3/2} \left(\frac{M_{\text{c}}}{2\,\text{M}_\odot}\right)^2 \left(\frac{M_{\text{s}}}{10\,\text{M}_\odot}\right)^{-7/2}\text{s}, \tag{6}$$

where α represents the viscosity, R_{s} and M_{s} the radius and mass of the WR star, and M_{c} is the mass of the compact object. For massive compact objects, an accretion time-scale of several tens of ks is not impossible.[6] According to Barkov & Kommisarov (2010), during accretion the compact object will produce jets via the Blandford–Znajek mechanism, and the jet luminosity will be in the range of 10^{49} erg s^{-1}, more than enough to explain the luminosity during

---

[6] Note, though, that equation (6) is valid if M_{c} is considerably smaller than M_{s}. However, if they become comparable, e.g. when we have a black hole of 10 M$_\odot$ and WR star of similar mass, one has to find a different method to estimate t_{d}.

the slow decline phase. None the less, this scenario might suffer from the same problems as the previous one. If the viscosity of the accretion disc is low, which is required to keep the material around the black hole for ~1 d, then the flux should not decrease quickly at the end of the plateau. The binary origin scenario could not reproduce the steep X-ray flux drop and/or it would require a peculiar structure of the WR star to explain the temporal dependence of the luminosity. We note, however, that in their papers, Barkov and Kommissarov do not discuss what happens at the end of the plateau, so we can only postulate.

Finally, we remark that this binary origin model can predict an SN, like the one associated with GRB 130831A.

4.2.6 Concluding remarks on the origin of the X-ray emission

We have shown that the FS scenario (or any refreshed shock scenario) cannot explain the X-ray emission of GRB 130831A between the end of prompt emission and ≃100 ks, since such a model cannot entail the steep decay of the flux at that epoch.

We have investigated whether such early X-ray emission can be attributed to dissipation processes occurring in the outflow of a newly born magnetar, produced via spin-down energy extraction of the compact object. We have found that the simplest model cannot explain the observations, because it predicts a flat X-ray light curve followed by a steep drop. In the case of GRB 130831A, the decay slope before the break is $\alpha \simeq 0.8$, which is much steeper than what we expect in this model. However, a more elaborate model of the magnetar spin-down, in which the magnetic field is expected to decay as the rotation time increases, predicts a luminosity decay more consistent with observations and a duration that can extend up to tens of ks. Moreover, the anticipated X-ray luminosity is in the right range. The assumed initial parameters – initial period P and magnetic field B – for the newly born magnetar that would produce such a X-ray light curve are $P = 1$–2 ms and $B \simeq 10^{15}$ G, which are expected on theoretical grounds for such an object.

We have also discussed whether the compact object could be a black hole rather than a magnetar. In order to power emission for such a long time, the black hole should be surrounded by an extended disc, perhaps produced by fall-back material of the SN associated with the GRB. While this model still may predict the right luminosity and duration for the 'internal' X-ray emission, it would require an anomalous distribution of angular momentum in the progenitor star, and peculiar fall-back rates. Similar advantages and disadvantages may be present in a model in which the compact object forms a binary with a WR star and spirals in, blowing up the star into a massive disc. All in all, we deem the magnetar model with a decaying magnetic field the most plausible of those presented so far to explain the properties of GRB 130831A.

4.3 Energy budget of the X-ray radiation between the end of the prompt emission and the 100 ks drop

In the cosmological rest frame, the X-ray internal emission begins no later than $200/(1 + 0.479) = 135$ s and lasts until $\simeq 98.2 \times 10^{3}/(1 + 0.479) \simeq 66.4 \times 10^{3}$ s. Taking into account cosmological corrections, the 0.3–10 keV luminosity at 135 s is 2.1×10^{47} erg s^{-1}; we assume that from this epoch the luminosity decreases as $t^{-0.8}$ up to 66.4 ks. We subtract the amount of X-ray emission produced by the FS (see Section 4.5), and we obtain a total energy $E_X \simeq 2.8 \times 10^{50}$ erg. Such a value represents $\simeq 2.5$ per cent of the energy emitted during the prompt phase, and only $\simeq 0.25$ per cent

of the kinetic energy of the relativistic ejecta producing the FS emission. We note, however, that the internal emission may extend below 0.3 and above 10 keV. Thus, E_X and the percentage we have determined represent a lower limit.

4.4 Energy breakdown of GRB 130831a and the associated SN

We know that the kinetic energy of the ejecta of SN 2013 fu, the SN associated with GRB 130831A, is $\simeq 1.9 \times 10^{52}$ erg (Cano et al. 2014). This is a factor ~6 lower than the kinetic energy of the relativistic ejecta and comparable to the energy emitted during the prompt emission, and ~60 times higher than the energy associated with the X-ray emission of 'internal origin'. We do caution, however, that the estimated SN kinetic energy is *isotropic*, while the energy of the relativistic ejecta, the prompt and the early X-ray energetics must be corrected for an unknown beaming factor. GRB 130831A does not show the signature of a jet break (Sari et al. 1999) within our observations, so we cannot derive the beaming angle θ_j of the ejecta and thus the beaming factor. However, we can set limits. The detection of the X-ray afterglow by *Chandra* at 1430 ks after the trigger indicates that the FS X-ray afterglow had a decay slope of $\simeq 1$ up to that epoch and no jet break had yet occurred.

Following Zhang & MacFadyen (2009), the beaming angle of the ejecta in a medium with constant density can be estimated as

$$\theta_{\rm jet} = 0.12 \left(\frac{t_{\rm jet,d}}{1+z} \right)^{3/8} \left(\frac{E_{\rm K,53}}{n} \right)^{-1/8} \text{ rad,} \qquad (7)$$

where $t_{\rm jet,\,d}$ is the jet break time in days. Our first *Chandra* observation took place 16.6 d after the trigger and we adopt the values E_K and n determined from our modelling; we note that the exact value of θ_j depends only weakly on the value of these parameters anyway. We infer that $\theta_j \gtrsim 0.123$ rad; thus the lower limit on the beaming factor is $f_b \simeq \theta_j^2/2 \simeq 7.56 \times 10^{-3}$. By definition, the maximum value for the beaming factor is $f_b = 1$ when the source is isotropic.

If the beaming factor of GRB 130831A emission were $f_b = 7.56 \times 10^{-3}$, the total energy budget of this event and its SN would be $\simeq 2.0 \times 10^{52}$ erg. The prompt energy E_γ, the energy emitted in X-rays up to 100 ks E_X, and the kinetic energy E_K of the relativistic ejecta would be $\simeq 0.4$, $\simeq 0.01$ and $\simeq 4.5$ per cent of the total energy budget. If, as an extreme and unlikely case, GRB 130831A were isotropic, its total energy budget would be 1.5×10^{53} erg; the above percentages would become $\simeq 7$, $\simeq 0.2$ and $\simeq 80$ per cent. The kinetic energy of the relativistic ejecta is *at least* $\simeq 4.5$ per cent of the total energy produced by the GRB and the SN. Moreover, the fraction of energy going into the 'internal emission' X-rays is always rather small, being substantially less than 1 per cent in both cases.

If GRB 130831A and its SN are powered by a magnetar, the total energy budget cannot be $\gtrsim 3 \times 10^{52}$ erg (see Section 4.2). To not exceed this limit, the beaming factor of the GRB must be $f_b \lesssim 0.1$. If $f_b = 0.1$, E_γ, E_X, and E_K represent $\simeq 3.3$, $\simeq 0.1$ and 37 per cent of the total energy. In reality, we should expect these percentages to be between those of the $f_b = 0.1$ and $f_b = 7.56 \times 10^{-3}$ cases if GRB 130831A is actually powered by a magnetar. The breakdown is presented again in Table 8.

4.5 Early afterglow

In our analysis, we have focused on the afterglow emission between 15 and 230 ks. It is worth exploring whether our model can explain the interesting features of the early afterglow, especially the optical band.

Table 8. Breakdown of energetics of GRB 130831A and its associated SN 2013 fu into energy emitted in gamma-rays E_γ, energy produced in X-rays of internal origin E_X, and kinetic energy associated with the relativistic GRB ejecta E_K. These values are corrected for beaming corresponding to the beaming factor f_b. The kinetic energy of the SN is $E_{SN} = 1.9 \times 10^{52}$ erg (Cano et al. 2014), and the total energy is $E_{tot} = E_{SN} + E_\gamma + E_X + E_K$.

Beaming factor f_b	$E_{tot, 52}$	$E_{\gamma, corr}$	E_X	E_K
1 (isotropic)	14.8	7.2 per cent	0.19 per cent	80 per cent
0.1 (magnetar limit)	3.2	3.3 per cent	0.09 per cent	37 per cent
7.56×10^{-3} (lower limit)	2.0	0.4 per cent	0.01 per cent	4.5 per cent

The initial flare peaks at 730 s. It takes place both in the X-ray and optical bands, but it is very pronounced in the latter. Its rapid temporal evolution (the optical flux increased by a factor of ∼5 between 400 and 800 s after the trigger) suggests that it could be explained in the context of internal dissipation processes which occurred in the outflow, when the Lorentz factor is very high and relativistic effects cause rapid variations of the observed flux. Thus, GRB 130831A may show a clear example of internal dissipation that produces strong emission in the optical other than in the X-ray. Alternatively, the optical flare might flag the onset of FS emission. However, if this were the case, the decay slope after the flare peak would be consistent with the decay slope of the late optical afterglow α_{opt}. Instead, the decay rate after the flare peak is $\alpha = 1.79 \pm 0.02$, which is inconsistent with $\alpha_{opt} = 1.59 \pm 0.03$ found later. After the flare, the early optical emission shows a plateau up to a few ks (see Section 3). Typically, an early slow optical decay is interpreted as energy injection, which ends at the time of the break. However, this interpretation might be difficult in our scenario, because the energy injection would have to stop at ∼5 ks while, according to our analysis, the GRB outflow is still active at ≃100 ks.

A possibility is that the optical plateau basically results from the combination of the decaying optical flare and the rising of the FS peak, which has been shown for a number of *Swift* bursts for which early optical light curves are available (Oates et al. 2009). The peak Lorentz factor Γ of the ejecta then can be calculated (Molinari et al. 2007 and references therein) as

$$\Gamma = 160 \left(\frac{E_{\gamma,53}(1+z)^3}{\eta_{0.2} n t_{dec,2}^3} \right)^{1/8}. \tag{8}$$

For a deceleration time $t_{dec} = 4000$ s and adopting the values of energy and density we have determined above, the resulting peak Lorentz factor would be $\Gamma \simeq 100$, which is within the overall distribution of Lorentz factors for GRB afterglows (Oates et al. 2009). The reason for such a late deceleration, in our model, comes naturally given the low density of the circumburst medium.

The late emission, which we attribute to FS in our modelling, seems to have a relatively steep decay slope. So one may wonder whether it could give some important contribution to the X-ray flux as well at an earlier epoch. If we extrapolate the late X-ray flux to earlier epochs using a decay slope of ≃1.6, it would become comparable to or even higher than the observed X-ray flux at the end of the first orbit (at ≃800 s) and the shape of the X-ray light curve would differ from what we see. However, if the FS onset occurs at ≃4000 s, this problem is avoided. As for the observations from ≃9 ks (i.e. the beginning of the second orbit) onwards, at 10 ks the flux by FS emission is $\simeq 6 \times 10^{-14}$ erg cm^{-2} s^{-1} $\times (\frac{10}{173})^{-1.59} = 5.5 \times 10^{-12}$ erg cm^{-2} s^{-1}, which is ∼3 times weaker than the observed X-ray flux. Afterwards, the FS flux decreases faster than that of 'internal origin' that we see, which decays with a slope of ≃0.8. Similarly, for a $\beta_{OX} = 1.03$ and flux density in the R-band (4.6 × 10^{14} Hz) of ≃410 μJy at 10 ks, the expected X-ray 0.3–10 keV flux is $\simeq 5.4 \times 10^{-12}$ erg

cm^{-2} s^{-1}. This is again ∼3 times lower than the X-ray flux observed at 10 ks. Thus, the X-ray flux from 9 ks up to the steep drop is not predominantly produced by the FS.

5 CONCLUSIONS

We have discussed the case of the long *Swift* GRB 130831A. The X-ray afterglow of this burst initially shows a shallow decay. However, at ≃100 ks the X-ray light curve breaks to an unusually steep decay slope ≃6, which cannot be explained by the standard FS model. Late XRT and especially *Chandra* observations show that the X-ray afterglow has a successive break to a more sedate decay with a slope ≃1.1.

The well-sampled optical afterglow shows no change of slope concurrent with the steep break in the X-ray band, which we interpret as arising from a different mechanism. By means of data taken by *Swift*, *Chandra* and several ground-based observatories, we have shown that both the optical and late X-ray emissions, after ≃200 ks after the trigger, have the typical decay and spectral slopes of GRB afterglows explained by the FS model.

We have interpreted the X-ray and optical afterglow as the superposition of two emission components. One component is of 'internal' origin, generated within a relativistic outflow and responsible for the early X-ray emission up to ≃100 ks; the outflow is produced by either the spin-down of a newly formed magnetar or a black hole feeding on fall-back matter. A second component, responsible for the late X-ray and optical from a few ks after the trigger, is the typical FS emission. When the magnetar has lost much of its rotational energy or the black hole does not accrete and does not power the outflow any longer, the first component dies off and we see the steep X-ray decay that lasts until the standard FS emission emerges. We believe that the magnetar model is favoured, since the other scenario would require a rather peculiar stellar progenitor structure and fall-back process.

Modelling the late optical and X-ray afterglow, we have inferred the kinetic energy of the relativistic ejecta and thus an efficiency $\eta \simeq 0.07$ of the 'central engine' of this GRB to produce gamma-ray emission. This efficiency is smaller than that of other bursts that show emission of internal origin (Lü & Zhang 2014; although these were examined in the X-ray band only), and more typical of those GRBs in which no internal emission is clearly visible. Thus, GRB 130831A may represent a 'trait d'union' between GRBs with different dominant emission processes.

More importantly, gathering the information on the kinetic energy of the SN associated with 130831A, we have provided a breakdown of the energetics of the GRB and its associated SN. We have found that, regardless of the nature of the central engine and unknown collimation of the ejecta, at least ≃4.5 per cent of the total energy of the event is coupled with relativistic ejecta; and less (probably significantly less) than ≃0.2 per cent of the energy goes into X-ray emission of 'internal origin' lasting up to 100 ks in our case; this

component produces a factor ~30 less energy than that released in gamma-ray during the prompt emission.

Showing several emission processes at work, GRB 130831A has offered us the opportunity to investigate the complete phenomenon of an SN with a central engine that produces the explosion and drives an energetic relativistic outflow, where dissipation processes take place for a long time.

REFERENCES

Ahn C. P., Alendandroff R., Allende-Prieto C., 2012, ApJS, 203, 21
Amati L., 2006, MNRAS, 372, 233
Amati L., Frontera F., Guidorzi C., 2009, A&A, 508, 173
Antoniadis J., Freire P., Wex C., 2013, Science, 508, 173
Arnaud K. A., 1996, in Jacoby G., Barnes J., eds, ASP Conf. Ser. Vol. 101, Astronomical Data Analysis Software and Systems V. Astron. Soc. Pac., San Francisco, p. 17
Band D. et al., 1993, ApJ, 413, 281
Barkov M., Komissarov S., 2010, MNRAS, 401, 1644
Barthelmy S. D. et al., 2005, SSR, 120, 143
Bernardini M. G. et al., 2014, MNRAS, 439, L80
Bertin E., Arnouts S., 1996, A&A, 117, 393
Bertin E., 2010, Astrophysics Source Code Library, record ascl:1010.063
Blandford R. D., Znajek R. L., 1977, MNRAS, 179, 433
Bloom J. S., Frail D. A., Sari R., 2001, AJ, 121, 2879
Breeveld A. A., Landsman W., Holland S. T., Roming P.; Kuin N. P. M.; Page M. J., 2011, in McEnery J. E., Racusin J. L., Gehrels N., eds, AIP Conf. Proc. Vol. 1358, Gamma Ray Bursts 2010. Am. Inst. Phys., New York, p. 373
Burrows D. N. et al., 2005, Space Sci. Rev., 120, 165
Butler N. et al., 2012, in McLean I. S., Ramsay S. K., Takami H., Proc. SPIE Conf. Ser. Vol. 8446, Ground-based and Airborne Instrumentation for Astronomy IV. SPIE, Bellingham, p. 844610
Cano Z., 2013, MNRAS, 434, 1098
Cano Z. et al., 2014, A&A, 568, 19
Cano Z. et al., 2015, MNRAS, 452, 1535
Cenko S. B. et al., 2011, MNRAS, 420, 2684
Cepa J. et al., 2000, in Iye M., Moorwood A. M. F., ed., Proc. SPIE Conf. Ser. Vol. 4008, Optical and IR Telescope Instrumentation and Detectors. SPIE, Bellingham, p. 623
Chandra P., Frail D. A., 2012, ApJ, 746, 156
Chevalier R. A., 1989, ApJ, 346, 847
Cucchiara A., Perley D., 2013, GCN Circ. 15144
Curran P. A., Evans P. A., De Pasquale M., Page M. J., van der Horst A. J., 2010, ApJ, 716, L135
Dall'Osso S., Stratta G., Guetta D., Covino S., De Cesare G., Stella L., 2011, A&A, 526, 121
De Ugarte Postigo A. et al., 2012, A&A, 538, A44
Duffel P. C., MacFadyen A., 2014, ApJ, 791, L1
Evans P. A., Beardmore A. P, Osborne J. P., Wynn G. A., 2009, MNRAS, 399, 1167
Falcone A. D. et al., 2007, ApJ, 671, 1921
Fruscione A. et al., 2006, in Silva D. R., Doxsey R. E., eds, Proc. SPIE Conf. Ser. Vol. 6270, Observatory Operations: Strategies, Processes, and Systems. SPIE, Bellingham, p. 62701V
Gehrels N., 1986, ApJ, 303, 336
Gehrels N. et al., 2004, ApJ, 611, 1005
Golenetskii S., Aptekar R., Fredericks D., Pal'Shin V., Oleynik P., Ulanov M., Svinkin D., Cline T., 2013, GCN Circ., 15145
Granot J., 2006, Rev. Mex. Astron. Astrofis., 270, 140
Greiner J. et al., 2015, Nature, 523, 189
Henden A., Munari U., 2014, Contrib. Astron. Obs. Skalnate Pleso, 43, 518
Hjorth J. et al., 2012, ApJ, 756, 187
Jarosik N. et al., 2011, ApJS, 192, 14
Jordi K., Grebel E. K., Ammon K., 2006, A&A, 460, 339
Kalberla P. M. W., Burton W. B, Hartmann D., Arnal E. M., Bajaja E., Morras R., Pöppel W. G. L., 2005, ApJ, 440, 775
Klein C. R. et al., 2012, 8453, 2
Klose S., Nicuesa Guelbenzu A., Krühler T., Greiner J., Kann D. A., Rau A., Olivares E. F., Schulze S., 2013, Central Bureau Electron. Telegrams, 3677, 1
Kobayashi S., Zhang B., 2007, ApJ, 655, 973
Komissarov S., Barkov M., 2009, MNRAS, 397, 1153
Kraft R. P., Burrows D. N., Nousek J. A., 1991, ApJ, 374, 344
Kumar P., Panaitescu A., 2000, ApJ, 541, 51
Kumar P., Narayan R., Johnson J. L., 2008, MNRAS, 388, 1729
Kumar P., Zhang B., 2015, Phys. Rep., 561, 1
Lang D., Hogg D. J., Mierle K., Blanton M., Roweis S., 2010, AJ, 139, 1782
Laskar T., Zauderer A., Berger E., 2013, GCN Circ. 15162
Liang E.-W. et al., 2006, ApJ, 646, 351
Liang E.-W., Zhang B.-B., Zhang B., 2007, ApJ, 670, 565
Lü H. J., Zhang B., 2014, ApJ, 785, 74
Lü H. J., Zhang B., Lei W.-H., 2015, ApJ, 805, 89
Lyons N., O'Brien P. T., Zhang B., Willingale R., Troja E., Starling R. L. C., 2010, MNRAS, 402, 705
MacFadyen A. I., Woosley S. E., 1999, ApJ, 524, 262
MacFadyen A. I., Woosley S. E., Heger A., 2001, ApJ, 550, 410

Margutti R., Bernardini G., Barniol-Duran R., Guidorzi C., Shen R. F., Chincarini G., 2011, MNRAS, 410, 1064

Matheson T. et al., 2003, ApJ, 599, 394

Metzger B. D., Giannios D., Thompson T. A., Bucciantini N., Quataert E., 2011, MNRAS, 413, 2031

Metzger B. D., Margalit B., Kasen D., Quataert E., 2015, preprint (arXiv:1508.02712)

Molinari E. et al., 2007, A&A, 469, 13

Molotov I. et al., 2008, Adv. Space Res., 41, 1022

Nousek J. A. et al., 2006 ApJ, 1, 389

Oates S. R. et al., 2009, MNRAS, 395, 490

O'Brien P. T. et al., 2006, ApJ, 647, 1213

Panaitescu A., Kumar P., 2002, ApJ, 571, 779

Pei Y.-C., 1992, ApJ, 395, 130

Perley D. A. et al., 2014, ApJ, 781, 37

Poole T. S. et al., 2008, MNRAS, 383, 627

Pozanenko A. et al., 2013, EAS Publ. Series, 61, 259

Racusin J. L. et al., 2009, ApJ, 698, 43

Reichart D. et al., 2005, Nuovo Cimento C, 28, 767

Rieger F., Bosch-Ramon F., Duffy P., 2007, Ap&SS, 309, 119

Roming P. W. A. et al., 2005, Space Sci. Rev., 120, 95

Rowlinson A., O'Brien P. T., Metzger B. D., Tanvir N. R., Levan A. J., 2013, MNRAS, 430, 1061

Sari R., Piran T., Halpern J. P., 1999, ApJ, 519, 17

Schlegel D. J., Finkbeiner D. P., Davis M., 1998, ApJ, 500, 525

Shen R.-F., Zhang B., 2009, MNRAS, 398, 1936

Swenson C. A., Roming P. W. A., De Pasquale M., Oates S. R., 2013 ApJ, 774, 2

Thompson T. A., 2007, Rev. Mex. Astron. Astrofis., 27, 80

Thompson T. A., Metzger B. D., Bucciantini N., 2010, in Kawai N., Nagataki S., eds, AIP Conf. Proc. Vol. 1279, Deciphering the Ancient Universe with Gamma Ray Bursts. Am. Inst. Phys., New York, p. 81

Tody D., 1986, in Crawford D. L., ed., Proc. SPIE Conf. Ser. Vol. 627, Instrumentation in Astronomy VI. SPIE, Bellingham, p. 733

Tody D., 1993, in Hanisch R. J., Brissenden R. J. V., Barnes J., eds, ASP Conf. Ser. Vol. 52, Astronomical Data Analysis Software and Systems II. Astron. Soc. Pac., San Francisco, p. 173

Troja E. et al., 2007, ApJ, 665, 599

Uhm Z. L., Zhang B., 2014, ApJ, 789, 39

Usov V. V., 1992, Nature, 357, 472

van Eerten H., Zhang W., MacFadyen A., 2010, ApJ, 722, 235

Vietri M., Stella L., 1998, ApJ, 507, 45

Volnova A., Matkin A., Stepura A., Molotov I., Pozanenko A., 2013a, GCN Circ. 15185

Volnova A., Linkov V., Polyakov K., Molotov I., Pozanenko A., 2013b, GCN Circ. 15188

Volnova A., Krugly Y., Slyusarev I., Molotov I., Pozanenko A., 2013c, GCN Circ. 15189

Watson A. M. et al., 2012, in Stepp L. M., Gilmozzi R., Hall H. J., ed., Proc. SPIE Conf. Ser. Vol. 8444, Ground-based and Airborne Telescopes IV. SPIE, Bellingham, p. 84445L

Woosley S. E., 2012, in Gamma-Ray Bursts. Cambridge Univ. Press, preprint (arXiv:1105.4193)

Woosley S. E., 1993, ApJ, 405, 273

Zauderer B. A., Laskar T., Berger E., 2013, GCN Circ. 15159

Zhang B., 2011, C. R. Phys., 12, 206

Zhang B., 2014, ApJL, 780, 2

Zhang B., Mészáros P., 2001, ApJ, 552, 35

Zhang B., Mészáros P., 2002, ApJ, 566, 712

Zhang B., Fan Y.-Z., Dyks J., Kobayashi S., Mészáros P., Burrows D. N., Nousek J. A., Gehrels N., 2006, ApJ, 642, 345

Zhang B. et al., 2007, ApJ, 655, 989

Zhang X.-H., 2009, Res. Astron. Astrophys., 9, 213

Zhang W.-Q., MacFadyen A., 2009, ApJ, 698, 1261

Zhang B., Yan H., 2011, ApJ, 726, 90

SUPPORTING INFORMATION

Additional Supporting Information may be found in the online version of this article:

Table 3. Photometry of the Afterglow of GRB 130831A. All magnitudes are in the Vega system (http://mnras.oxfordjournals.org/lookup/suppl/doi:10.1093/mnras/stv2280/-/DC1).

Please note: Oxford University Press is not responsible for the content or functionality of any supporting materials supplied by the authors. Any queries (other than missing material) should be directed to the corresponding author for the article.

[1]*Mullard Space Science Laboratory, University College London, Dorking, RH5 6NT, UK*

[2]*Istituto Astrofisica Spaziale Fisica Cosmica, Palermo 90146, Italy*

[3]*Istituto Euro Mediterraneo di Scienza e Tecnologia, Palermo 90139, Italy*

[4]*Istituto de Astrofisica de Andalucia (CSIC), Granada E-18008, Spain*

[5]*Center for Research and Exploration in Space Science And Technology (CRESST) and NASA Goddard Space Flight Center, Greenbelt, MD 20771, USA*

[6]*Thüringer Landessternwarte Tautenburg, Sternwarte 5, D-07778 Tautenburg, Germany*

[7]*Department of Physics and Astronomy, University of Nevada Las Vegas, Las Vegas NV 89154, USA*

[8]*Space Research Institute (IKI), Moscow 117997, Russia*

[9]*National Research Nuclear University MEPhI (Moscow Engineering Physics Institute), 115409 Moscow, Russia*

[10]*University of North Carolina at Chapel Hill, Chapel Hill, North Carolina NC 27599, USA*

[11]*Pennsylvania State University, University Park, PA 16802, USA*

[12]*Arizona State University, Tempe, AZ 85281, Arizona, USA*

[13]*Instituto de Astrofísica, Facultad de Física, Pontificia Universidad Católica de Chile, Vicuña Mackenna 4860, 7820436 Macul, Santiago, Chile*

[14]*Millennium Institute of Astrophysics, Vicuña Mackenna 4860, 7820436 Macul, Santiago, Chile*

[15]*Centre for Astrophysics and Cosmology, Science Institute, University of Iceland, 107 Reykjavik, Iceland*

[16]*Unidad Asociada Departamento de Ingenieria de Sistemas y Automatica, Universidad de Malaga, MÁlaga, 29071, Spain*

[17]*Unidad Asociada Grupo Ciencia Planetarias UPV/EHU-IAA/CSIC, Departamento de Física Aplicada I, E.T.S. Ingeniería, Universidad del País Vasco UPV/EHU, Alameda de Urquijo s/n, E-48013 Bilbao, Spain*

[18]*Ikerbasque, Basque Foundation for Science, Alameda de Urquijo 36-5, E-48008 Bilbao, Spain*

[19]*Department of Physics, University of Maryland, Baltimore County, Baltimore, MD 21250, USA*

[20]*University of California Berkeley, Berkeley, CA 94720, USA*

[21]*University of California Santa Cruz, Santa Cruz, CA 95064, USA*

[22]*Instituto de Astronomía, Universidad Nacional Autónoma de México, Apartado Postal 70-264 04510 México, DF, Mexico*

[23]*Instituto de Astronomía, Universidad Nacional Autonoma de México, Apartado Postal 106, 22800 Ensenada, Baja California, Mexico*

[24]*The University of Chicago, Chicago, IL 60637, USA*

[25]*Crimean Astrophysical Observatory, 98409 pgt. Nauchny, Crimea*

[26]*Institute of Solar-Terrestrial Physics, Russian Academy of Sciences, 664033, p/o box 291; Lermontov st, 126a Irkutsk, Russia*

[27]*Ulugh Beg Astronomical Institute, 100052, 33 Astronomicheskaya str., Tashkent, Uzbekistan*

This paper has been typeset from a TEX/LATEX file prepared by the author.